# MODEL-BASED IMAGE PROCESSING ALGORITHMS FOR CT IMAGE RECONSTRUCTION, ARTIFACT REDUCTION AND SEGMENTATION

A Dissertation

Submitted to the Faculty

of

Purdue University

by

Pengchong Jin

In Partial Fulfillment of the

Requirements for the Degree

of

Doctor of Philosophy

August 2015

Purdue University

West Lafayette, Indiana

# ACKNOWLEDGMENTS

I would like to express my sincerely appreciation to my PhD advisor, Prof. Charles A. Bouman, for his education and support. Prof. Bouman is an outstanding reseaercher, an excellent teacher and a great friend. His passion about research and science, his attitude towards perfection, and his advices on not only being a top engineer but more importantly a great person, have always been inspiring me a lot. I would also like to thank Prof. Ken D. Sauer from University of Notre Dame for being one of my research collaborators, who has given me countless advises. I am also grateful for Dr. Yaowu Xu and Ms. Yueqing Wang from Google Inc., who hosted me a great internship in summer 2014. I would also like to thank Prof. Jan P. Allebach, Prof. Mark R. Bell and Prof. Mary L. Comer for serving as my thesis committee members.

The six-year study at West Lafayette is a remarkable experience in my life. I thank my colleagues in Integrated Imaging Lab at Purdue, including Eri Haneda, S. Jordan Kisner, Leonardo Bachega, Yandong Guo, Haitao Xue, Ruoqaio Zhang, Singanallur Venkatakrishnan and Dong Hye Ye for their discussions and support. I also thank my friends, Lingxing Zheng, Xinyue Chang, Na Wu, Rong Fu, Jason Chan, Yuetao Guo, for accompanying me during my spare time.

Last but not least, I thank for the enormous support from my family. I would like to express my gratitude to my parents, Mr. Guangye Jin and Ms. Fuwei Sun, for their love, encouragement and education in my life. Finally, the special thank goes to my wife, Wei Zheng, for her love, support, and everything that she has done for me. I owe my family a lot and dedicate my thesis to them.

TABLE OF CONTENTS

Page

# LIST OF TABLES

# LIST OF FIGURES

Figure Page

Figure Page

# ABSTRACT

Jin, Pengchong Ph.D., Purdue University, August 2015. Model-Based Image Processing Algorithms for CT Image Reconstruction, Artifact Reduction and Segmentation. Major Professor: Charles A. Bouman.

Model-based image processing is a collection of techniques that provides a systematic framework for solving inverse problems in imaging systems. In this dissertation [1], three problems that arise in CT imaging systems are addressed using the model-based approach: image reconstruction for the single energy X-ray CT with both 2D parallel-beam and 3D multi-slice geometries, simultaneous image reconstruction and beam hardening correction for the single energy X-ray CT, and simultaneous metal artifact reduction and image segmentation for CT images.

In the first topic, the methodology of model-based iterative reconstruction (MBIR) for solving CT image reconstruction problems is studied. Recent research indicates that the MRIR has potential to improve image quality and remove artifacts comparing to traditional filtered back-projection (FBP) methods. The MBIR algorithms for both 2D parallel-beam and 3D multi-slice helical CT geometries are developed using the formulation under the statistical framework and the reconstruction is solved using optimization techniques. The result on the real CT baggage dataset is presented, which illustrates the image quality improvement and noise and artifact reduction.

The second topic studies the beam hardening correction problem in the single-energy X-ray CT. Beam hardening is the effect that material preferably attenuates more low-energy X-ray than high-energy, and with a broad X-ray source spectrum,

[1] This material is based upon work supported by the U.S. Department of Homeland Security, Science and Technology Directorate, Office of University Programs, under Grant Award 2013-ST-061-ED0001. The views and conclusions contained in this document are those of the authors and should not be interpreted as necessarily representing the official policies, either expressed or implied, of the U.S. Department of Homeland Security.

it can lead to several reconstructed image artifacts, such as streaks. Based on the assumption that distinct materials can be separated according to their densities, a more accurate forward model that accounts for the X-ray spectrum is developed and a MBIR algorithm that incorporates this new model is proposed. The overall algorithms works by alternating estimation of the image and the unknown model parameters, therefore no additional information is required. Results on both the simulated and real CT scan data show that the proposed method significantly reduces metal streak artifacts in the reconstruction.

The third problem is the segmentation of CT images with metal artifacts and without the access to the CT data. Segmenting interesting objects from CT images has a wide range of applications in medical diagnosis and security inspection. However, raw CT images often contain artifacts such as streak due to the dense metal objects, and these artifacts can make accurate segmentation difficult. A novel model-based approach that jointly estimates both the segmentation and the restored image is proposed and the unified cost function consists of three terms: 1) a data fidelity term that relates the raw and restored image and incorporates a streak mask; 2) a dictionary-based image prior which regularizes the restored image; 3) a term based on the continuous-relaxed Potts model which couples the restored image intensities and segmentation labels. Results on both simulated and real CT data are presented and support that the joint segmentation and MAR can produce superior results without the use of the raw CT data.

# 1. MODEL-BASED ITERATIVE RECONSTRUCTION (MBIR) FOR X-RAY CT SYSTEMS

## 1.1 Introduction

X-ray Computed Tomography (CT) has been widely used in medical diagnosis and security inspection. However, the more complex and advanced system hardware, as well as the higher demand of the low dose scan requirement, pose challenges for image reconstructions. For example, unlike the parallel-beam CT scanner, the recent developed multi-slice helical CT scanner has the more complicated 3D scanner geometry, and as cone angles become wider, there is an increasing need to use true 3D reconstruction methods in order to avoid the image artifacts introduced by 2D approximations.

Model-based iterative reconstruction (MBIR) is a family of reconstruction methods under the model-based image processing framework, which has been shown to be effective in many imaging modalities, such as CT [1], PET, and MRI. These algorithms have the advantage that they can incorporate more detailed models of both the scanner and the objects being reconstructed. In addition, they offer more flexibility in various new applications since they allow for more accurate reconstruction for non-traditional geometries. Model-based algorithms have the potential to more accurately account for a wide array of scanner characteristics including photon counting and electronic noise, beam hardening, metal attenuation ans scanner, and the detector point spread function. More accurate modeling of the scanner can be used to reduce streak artifacts from high density objects. In addition, MBIR methods incorporates a prior model that can be tuned to the characteristics of typical objects and the performance metrics of interest.

In this chapter, we discuss the methodoloty of MBIR approach to CT image reconstruction. The approach is based on the maximum a posterior (MAP) estimation of the CT image under the optimization framework. We develop the forward models that accurately accounts for X-ray transmission statistics, X-ray projections for CT scanners with different geometries, and the prior model of the reconstructed images which regularize the local image structures. We also develop the iterative optimization method to solve the optimization problem and demonstrate how the algorithm can be parallelized on the multi-core processing hardware. We apply the algorithm on the real 3D multi-slice helical scan data of travel bags packed with a variety of high and low density objects and our results indicate that MBIR has the potential to produce reconstructions with few artifacts than analytic reconstruction methods.

## 1.2 Statistical Image Reconstruction Framework

Let $y \in \mathbb{R}^M, \{y_i : i = 1, \cdots, M\}$ be the sinogram measurement generated by the CT system, $x \in \mathbb{R}^N, \{x_j : j = 1 \cdots, N\}$ be the underlying image to be estimated. Here $M$ specifies the number of distinct X-ray measurements during data acquisition, and $N$ specifies the number of voxels in the reconstructed image volume.

In order to fully characterize the randomness of the underlying physical world, we assume that both the image $X$ and the measurement $Y$ are random, and the sinogram data $y$ is one particular realization of $Y$. MBIR computes the "best" reconstructed image in probability sense as the maximum a posterior (MAP) estimate of $X$ given $Y = y$, given by

$$\hat{x} = \arg\max_{x \in \Omega} \mathbb{P}(x|y) \tag{1.1}$$

where $\Omega$ is the feasible set of $x$. Applying the Bayes rule to (1.1) and taking the log, we obtain the common form of the estimation problem,

$$\begin{aligned} \hat{x} &= \arg\max_{x \in \Omega} \left\{ \frac{\mathbb{P}(y|x)\mathbb{P}(x)}{\mathbb{P}(y)} \right\} \\ &= \arg\max_{x \in \Omega} \{\log \mathbb{P}(y|x) + \log \mathbb{P}(x) - \log \mathbb{P}(y)\} \\ &= \arg\max_{x \in \Omega} \{\log \mathbb{P}(y|x) + \log \mathbb{P}(x)\} \ . \end{aligned} \tag{1.2}$$

The likelihood function $\mathbb{P}(y|x)$ characterizes the measurement $y$ given the image $x$, and it incorporates the system geometry, X-ray projection model, and measurement noise. $\mathbb{P}(y|x)$ may be different depending on applications. For example, a simple model assumes that $y$ is linearly related to $x$ while some other models will use high-order approximations to account for effects in various situations. The image prior distribution $\mathbb{P}(x)$ encodes the prior knowledge of what $x$ should behave like and it plays an important role of regularizing the estimation. For example, a prior on image may imposes the smoothness and consistency on local structures, in order to mitigate the effect introduced by the sparse and noisy data.

In the following sections, we develop the mathematical formulation of the generic MBIR algorithm for the single-energy X-ray CT system. Section 1.3 presents the noise model for the CT measurement based on X-ray transmission statistics. Section 1.4 derives the generic X-ray forward projection models for 2D parallel-beam and 3D multi-slice helical CT systems based on their specific geometries. Section 1.5 introduces a generic edge-preserving image prior commonly used in MBIR. Section 1.6 derives the iterative algorithm to solve the overall optimization problem.

## 1.3 X-ray Transmission Statistics

CT scanners do not measure the line integral of the object attenuation directly, but rather record the X-ray photon counts at the detector. Consider the single-energy X-ray CT scanner, where X-ray beams pass through the scanned object and the photon counts are received and recorded at the detector. Denote $\Lambda \in \mathbb{R}^M, \{\Lambda_i : i = 1, \cdots, M\}$ as the photon measurement. The CT sinogram measurement $Y$ is generated from $\Lambda$ using the negative logarithm transform, given by

$$Y_i \triangleq -\log\left(\frac{\Lambda_i}{\lambda_{T,i}}\right) \tag{1.3}$$

where $\lambda_{T,i}$ is the received photon counts in the air calibrated scan.

One simple assumption on the received X-ray photon counts $\Lambda_i$ is that it follows the Poisson distribution, given by

$$\Lambda_i|x \triangleq \text{Poisson}(\bar{\lambda}_i) \tag{1.4}$$

where $\bar{\lambda}_i$ is the mean (also the variance) of the Possion random variable, i.e.

$$\mathbb{E}[\Lambda_i|x] = \text{Var}[\Lambda_i|x] = \bar{\lambda}_i \ . \tag{1.5}$$

Using (1.5) and applying it to (1.3), we can derive the mean and variance of $Y_i$ mathematically. In particular, the mean of $Y_i$ is given by

$$\mathbb{E}[Y_i|x] = -\mathbb{E}\left[\log\left(\frac{\Lambda_i}{\lambda_{T,i}}\right)\right] \approx -\log\left(\frac{\mathbb{E}[\Lambda_i|x]}{\lambda_{T,i}}\right) = -\log\left(\frac{\bar{\lambda}_i}{\lambda_{T,i}}\right) \tag{1.6}$$

where the left side of the approximation in 1.6 is greater due to Jensen's inequality and the variance of $Y_i$ is given by

$$\text{Var}[Y_i|x] \approx \left(-\frac{\frac{1}{\lambda_{T,i}}}{\frac{\mathbb{E}[\Lambda_i|x]}{\lambda_{T,i}}}\right)^2 \text{Var}[\Lambda_i|x] = \frac{1}{\bar{\lambda}_i} \tag{1.7}$$

where we have used the approximation that for an arbitrary random variable $Z$, we have

$$\text{Var}[f(Z)] \approx \left(f'(\mathbb{E}[Z])\right)^2 \text{Var}[Z] \ . \tag{1.8}$$

In summary, the mean of $Y_i$ is the negative log of the normalized received photon counts, and its variance is inversely proportional to the received photon count.

However, the model above does not account for the electronic noise occurring at the photon counting detector. A better model assumes that the received photon counts is the sum of a Poisson random variable and an independent zero mean additive Gaussian noise, such that

$$\Lambda_i \triangleq \text{Poisson}(\bar{\lambda}_i) + \mathcal{N}(0, \sigma_e^2) \tag{1.9}$$

where $\sigma_e^2$ is the variance of the electronic noise. Therefore, we have

$$\mathbb{E}[\Lambda_i|x] = \bar{\lambda}_i \ , \tag{1.10}$$

$$\text{Var}[\Lambda_i|x] = \bar{\lambda}_i + \sigma_e^2 \ . \tag{1.11}$$

Substituting (1.10) and (1.11) into (1.3), we have the statistics of $Y_i$ given by

$$\mathbb{E}[Y_i|x] = -\log\left(\frac{\bar{\lambda}_i}{\lambda_{T,i}}\right) , \tag{1.12}$$

$$\mathrm{Var}[Y_i|x] = \frac{\mathrm{Var}[\Lambda_i|x]}{(\mathbb{E}[\Lambda_i|x])^2} = \frac{\bar{\lambda}_i + \sigma_e^2}{\bar{\lambda}_i^2} . \tag{1.13}$$

The model has the same mean as in (1.6) but incorporates the uncertainty of measurement $Y_i$ due to electronic noise into (1.13).

To further develop the expression of the likelihood function, we assume the sinogram measurement $Y_i$ are conditionally independent Gaussian. As a result, the log likelihood function in (1.3) can be written as

$$\log \mathbb{P}(y|x) \simeq -\frac{1}{2}(y - \mathbb{E}[Y|x])^T D(y - \mathbb{E}[Y|x]) + C \tag{1.14}$$

where $D$ is the diagonal matrix such that

$$D_{i,i} = \frac{1}{\mathrm{Var}[Y_i|x]} \tag{1.15}$$

representing the statistical weights of the $i$-th projection and $C$ is the normalizing function which does not depend on $x$. Notice that such approximation is fully justified by a second order Taylor's series expansion [2] in the case when the electronic noise is not considered. In Section 1.4, we continue to develop the generic X-ray forward projection model used for $\mathbb{E}[Y_i|x]$ in (1.14).

## 1.4 Generic X-ray Forward Projection Model

We next present the approach to formulate a generic X-ray forward projection model for $\mathbb{E}[Y_i|x]$.

Recall that according to the Lambert-Beer's law in X-ray physics, the rate of X-ray absorption is proportional to the intensity of the X-ray. Denote $I(r)$ to be the X-ray intensity at location $r$, the Lambert-Beer's law can be expressed as

$$\frac{d}{dr}I(r) = -\mu(r)I(r) \tag{1.16}$$

where $\mu(r)$ is the absorptive rate, known as the linear attenuation coefficient of the material, at location $r$. Therefore, if the incident X-ray intensity is $I_T$, then the received X-ray intensity after traversing the absorptive material, will be

$$I = I_T e^{-\int_{\text{ray}} \mu(r)dr} \tag{1.17}$$

where the exponent is the negative line integral of the linear attenuation coefficients through the particular line along which the X-ray beam passes.

Following the result from (1.17), we can model the mean of the received photon counts $\Lambda_i$ of the $i$-th projection as

$$\mathbb{E}[\Lambda_i|\mu] = \lambda_{T,i} e^{-\int_{\text{ray}} \mu(r)dr} \ . \tag{1.18}$$

However, as we can see from (1.18), it assumes that the received photo counts of the $i$-th projection is obtained from the single X-ray beam. In reality, each detector receives multiple X-ray beams and the recorded photon counts will be a sum of all the beams that hit the detector. Therefore, if we assume the incident X-ray intensities are the same for those beams that reach the detector, the expected value of the photon counts of the $i$-th projection will be

$$\mathbb{E}[\Lambda_i|\mu] = \lambda_{T,i} \int_{\chi_i} e^{-\int_{\text{ray}} \mu(r)dr} \tag{1.19}$$

where we use $\chi_i$ to denote the set of all the rays that hit the detector corresponding to the $i$-th detector. Using (1.19) and applying it to (1.12), we have

$$\begin{aligned} \mathbb{E}[Y_i|\mu] &= -\log\left(\frac{\lambda_{T,i}\int_{\chi_i} e^{-\int_{\text{ray}} \mu(r)dr}}{\lambda_{T,i}}\right) = -\log\left(\int_{\chi_i} e^{-\int_{\text{ray}} \mu(r)dr}\right) && (1.20) \\ &\approx -\int_{\chi_i} \log\left(e^{-\int_{\text{ray}} \mu(r)dr}\right) = \int_{\chi_i}\int_{\text{ray}} \mu(r)dr && (1.21) \end{aligned}$$

where the approximation in (1.21) is "less than" because of the Jensen's inequality. In summary, (1.21) says that the $i$-th sinogram measurement is the sum of the line integrals of the attenuation coefficients along all the rays that reach the detector corresponding to the $i$-th projection.

We further consider the discretization of the continuous attenuation map $\mu(r)$ using $x \in \mathbb{R}^N$. In particular, we assume that $\mu(r)$ can be expressed by $x$ over the uniform image grid as

$$\mu(r) = \sum_{j=1}^{N} x_j u_j(r) \tag{1.22}$$

where $x_j$ represents the average linear attenuation coefficient of the $j$-th pixel in the image grid, such that

$$x_j = \frac{\int_{\Upsilon_j} \mu(r) dr}{\int_{\Upsilon_j} dr} \tag{1.23}$$

where $\Upsilon_j$ specifies the $j$-pixel in the space, and $u_j(r)$ is the spatial function representing the normalized distribution of the linear attenuation at the $j$-th pixel, such that

$$u_j(r) = \begin{cases} \frac{\mu(r)}{x_j} & \text{if } r \in \Upsilon_j \\ 0 & \text{otherwise} \end{cases} \tag{1.24}$$

A simple approximation assumes $u(r)$ is unity at the $j$-th pixel and zero otherwise, i.e.

$$u_j(r) = \begin{cases} 1 & \text{if } r \in \Upsilon_j \\ 0 & \text{otherwise} \end{cases} \tag{1.25}$$

Using (1.22), we eventually relate the sinogram measurement $y$ and the image $x$ as a linearized transformation, given by

$$\mathbb{E}[Y_i|x] = \int_{\chi_i} \int_{\text{ray}} \mu(r) dr = \int_{\chi_i} \int_{\text{ray}} \sum_{j=1}^{N} x_j u_j(r) dr \tag{1.26}$$

$$= \sum_{j=1}^{N} x_j \int_{\chi_i} \int_{\text{ray}} u_j(r) dr = \sum_{j=1} A_{i,j} x_j \tag{1.27}$$

where we let $A \in \mathbb{R}^{M \times N}$ be the transformation matrix and its entry $A_{i,j}$ is defined as

$$A_{i,j} = \int_{\chi_i} \int_{\text{ray}} u_j(r) dr \ . \tag{1.28}$$

In particular, if we use the uniform pixel distribution $u(r)$ in (1.25), we have

$$A_{i,j} = \int_{\chi_i} \int_{\text{ray}, r \in \Upsilon_j} dr \ , \tag{1.29}$$

which essentially says that $A_{i,j}$ is the sum of the length of intersections of all the rays that hit the detector corresponding to the $i$-th projection with the $j$-th pixel location.

Substituting (1.27) into (1.14), we obtain the log likelihood function using the generic linearized X-ray forward projection model, as

$$\log \mathbb{P}(y|x) = -\frac{1}{2}(y - Ax)^T D(y - Ax) + C \ . \tag{1.30}$$

Our objective next is to derive the specific expression of $A_{i,j}$ in cases of 2D parallel-beam and 3D multi-slice helical CT, which complete our discussion of the X-ray forward projection model in MBIR.

### 1.4.1 2D Parallel-Beam CT

In this section, we develop the specific expression of the forward projection matrix $A_{i,j}$ for 2D parallel-beam CT. The parallel-beam geometry in 2D coordinate system is shown in Figure 1.1, where we use $(r_x, r_y)$ to denote the Cartesian coordinate of the 2D plane. $(\theta, t)$ as the polar coordinate for the projection X-ray beams, and we denote $\Delta_{xy}$ and $\Delta_d$ as the width of the pixel and detector respectively. We further translate the projection angle $\theta$ using

$$\tilde{\theta} = \left(\theta + \frac{\pi}{4}\right) \mod \frac{\pi}{2} - \frac{\pi}{4} \tag{1.31}$$

to ensure $|\tilde{\theta}| < \frac{\pi}{4}$ and simplify the trigonometric calculation following.

In 2D parallel-beam geometry, for the $i$-th projection, the projection angle is $\theta_i$ and all the X-ray beams that pass through point $(r_x, r_y)$ can be parametrized by $t$ using

$$r_x \sin\tilde{\theta}_i + r_y \cos\tilde{\theta}_i - t_i = 0 \ . \tag{1.32}$$

Therefore, if the detector corresponding to the $i$-th projection covers $[T_i^{\text{start}}, T_i^{\text{end}}]$ in $t$-direction, we could express the integral in (1.28) as

$$A_{i,j} = \int_{T_i^{\text{start}}}^{T_i^{\text{end}}} \int\int u_j(r_x, r_y)\delta(t - r_x \cos\tilde{\theta}_i - r_y \sin\tilde{\theta}_i) dr_x dr_y dt \ . \tag{1.33}$$

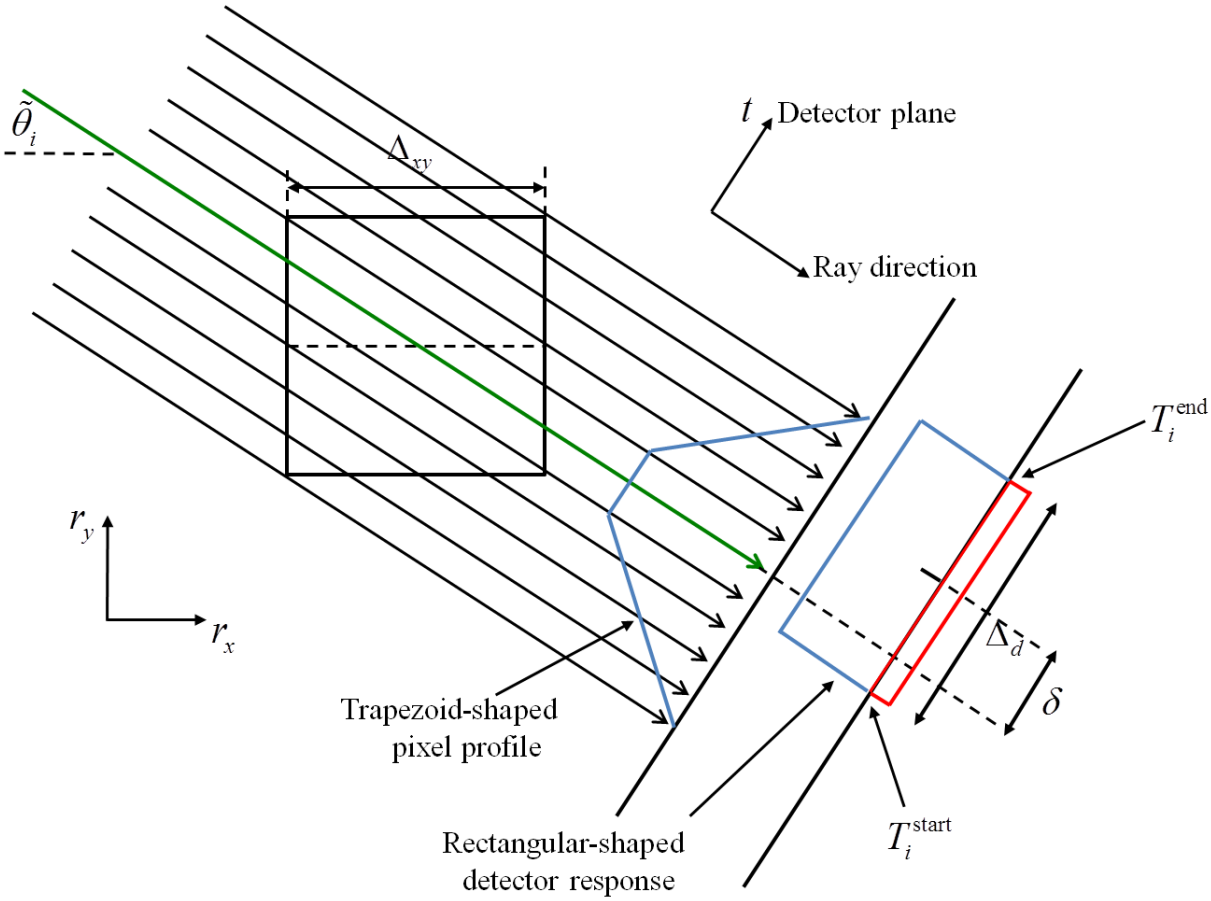


Fig. 1.1.: 2D geometry of multi-slice helical CT

Furthermore, one could generalize (1.33) and add the effect of detector sensitivity. In particular, we model the sensitivity of the detector corresponding to the $i$-th projection as $D_i(t)$, then the sinogram measurement can be written as

$$A_{i,j} = \int_{T_i^{\text{start}}}^{T_i^{\text{end}}} D_i(t) \int\int u_j(r_x, r_y)\delta(t - r_x\cos\tilde{\theta}_i - r_y\sin\tilde{\theta}_i)dr_x dr_y dt \ . \tag{1.34}$$

To reduce the computation complexity, we use the unity assumption (1.25) on $u_j(r_x, r_y)$, and the sinogram measurement can be simplified as

$$A_{i,j} = \int_{T_i^{\text{start}}}^{T_i^{\text{end}}} D_i(t) \int\int_{(r_x,r_y)\in\Upsilon_j} \delta(t - r_x\cos\tilde{\theta}_i - r_y\sin\tilde{\theta}_i)dr_x dr_y dt \ . \tag{1.35}$$

Notice that in the above formula (1.35), the inner double integral is just the width of intersection of a particular X-ray with the $j$-th pixel. Illustrated in Figure 1.1, we

could form a 1D function $P_j(t)$ along the $t$-axis, called the $j$-th pixel profile, whose function value are the width of intersection of all the rays with the $j$-th pixel, given by

$$P_j(t) = \int\int_{(r_x,r_y)\in\Upsilon_j} \delta(t - r_x\cos\tilde{\theta}_i - r_y\sin\tilde{\theta}_i)dr_x dr_y \ . \tag{1.36}$$

Using this definition, it turns out that the value of $A_{i,j}$ is just the inner product of $D_i(t)$ and $P_j(t)$, given by

$$A_{i,j} = \int_{T_i^{\text{start}}}^{T_i^{\text{end}}} D_i(t)P_j(t)dt \ . \tag{1.37}$$

Typically, we assume the uniform sensitivity for the detector, which leads to a rectangular-shaped $D_i(t)$. Also notice that assuming the uniform pixel distribution, $P_j(t)$ will be trapezoid-shaped. If we further translated both functions such that they become symmetric with respect to $t = 0$ and name the newly-translated functions as $\tilde{D}_i(t)$ and $\tilde{P}_j(t)$, then the calculation of $A_{i,j}$ is the convolution of two translated functions, evaluated at $t = \delta$, where $\delta$ is the width between the projected pixel center and detector center along the $t$-direction, i.e.

$$A_{i,j} = \tilde{D}_i(t) \star \tilde{P}_j(t) \mid_{t=\delta} = \int_{-\infty}^{\infty} \tilde{D}_i(\delta - \tau)\tilde{P}_j(\tau)d\tau \tag{1.38}$$

and mathematically, $\tilde{P}_j(t)$ and $\tilde{D}_i(t)$ can be written as

$$\begin{aligned} P_j(t) &= \text{Trapezoid}(\frac{\Delta_{xy}}{\cos\tilde{\theta}}, z_1, z_2) \\ &= \begin{cases} -\frac{1}{\sin\tilde{\theta}\cos\tilde{\theta}}(t - z_2), & z_1 < t < z_2 \\ \frac{\Delta_{xy}}{\cos\tilde{\theta}}, & |t| \le z_1 \\ \frac{1}{\sin\tilde{\theta}\cos\tilde{\theta}}(t + z_2), & -z_2 < t < -z_1 \\ 0, & \text{otherwise} \end{cases} \end{aligned} \tag{1.39}$$

where

$$z_1 = \frac{\Delta_{xy}}{2}\cos\tilde{\theta}(1 - \tan\tilde{\theta}) \tag{1.40}$$

$$z_2 = \frac{\Delta_{xy}}{2}\cos\tilde{\theta}(1 + \tan\tilde{\theta}) \tag{1.41}$$

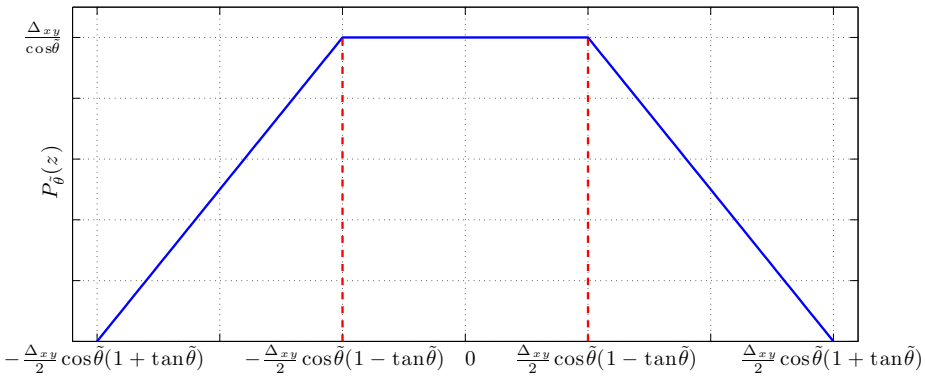


(a) $\tilde{P}_j(t)$

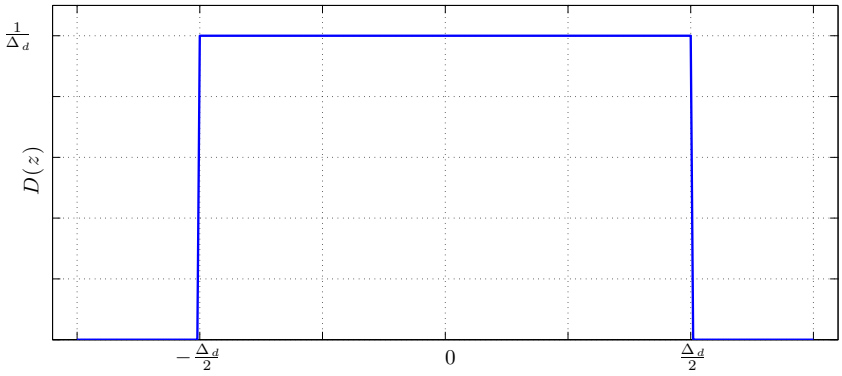


(b) $\tilde{D}_i(t)$

Fig. 1.2.: Illustration of the trapezoid-shaped pixel profile $\tilde{P}_j(t)$ and the rectangular-shaped detector response $\tilde{D}_i(t)$.

and

$$D_i(t) = \frac{1}{\Delta_d}\text{rect}\left(\frac{\Delta_d}{2}\right) = \begin{cases} \frac{1}{\Delta_d}, & |t| \leq \frac{\Delta_d}{2} \\ 0, & \text{otherwise} \end{cases} . \tag{1.42}$$

Figure 1.2 illustrates the shapes of the pixel profile and the detector response.

### 1.4.2 3D Multi-slice Helical CT

In the case of 3D multi-slice helical CT, the geometry is different. However, the basic idea is the same. In particular, we have the 3D analogy to the 2D equation (1.34), given by

$$A_{i,j} = \int_{\chi_i} D_i(x,y,z) \int\int\int u_j(x,y,z)\delta(L(x,y,z))dxdydz \tag{1.43}$$

where we use $(x,y,z)$ to denote the 3D Cartesian coordinate system, and we use $L(x,y,z)$ to represent abstractly the line in 3D space. Note that the coordinate $(x,y,z)$ should not be confused with the realization of random variable $X$ and $Y$ and the notation is only used in this section for derivation purpose.

To simplify the calculation, we first assume the separable properties for $\chi_i$, $D_i(x,y,z)$, $u_j(x,y,z)$ and $L(x,y,z)$. In particular, we decompose (1.43) as

$$\begin{aligned} A_{i,j} &= \int_{\chi_i^{xy}\times\chi_i^z} D_i(x,y)D_i(z) \int\int\int u_j(x,y)u_j(z)\delta(L(x,y))\delta(L(z)))dxdydz \\ &= \left(\int_{\chi_i^{xy}} D_i(x,y) \int\int u_j(x,y)\delta(L(x,y))dxdy\right)\left(\int_{\chi_i^z} D_i(z)\delta(L(z))dz\right) \\ &= B_{i,j} \times C_{i,j} \end{aligned} \tag{1.44}$$

where on the $xy$-plane, we define the coefficient $B_{i,j}$ as

$$B_{i,j} = \int_{\chi_i^{xy}} D_i(x,y) \int\int u_j(x,y)\delta(L(x,y))dxdy = \int_{\chi_i^{xy}} D_i(x,y)P_j(x,y)dxdy \tag{1.45}$$

and along the $z$-direction, we have the factor $C_{i,j}$ as

$$C_{i,j} = \int_{\chi_i^z} D_i(z) \int\int u_j(z)\delta(L(z))dz = \int_{\chi_i^z} D_i(z)P_j(z)dz \tag{1.46}$$

and $P_j(x,y)$ and $P_j(z)$ are the $j$-th voxel profile on the $xy$-plane and $z$-direction respectively.

As shown in Figure 1.3, for 3D multi-slice helical CT scanner, the detector array is not a flat plane and each detector element is arc-shaped. We use the simplified assumption that every detector element is flat and resides on the plane that is tangential to the center of that detector. As a result, we could apply the similar approach

in 2D case to $xy$-plane and $z$-plane, where the coefficients will be the inner product of two 1D functions, the pixel profile and the detector sensitivity, given by

$$\begin{aligned} B_{i,j} &= \int_{T_i^{\text{start}}}^{T_i^{\text{end}}} D_i(t)P_j(t)dt \\ &= \tilde{D}_i(t) \star \tilde{P}_j(t) \mid_{t=\delta_c} = \int_{-\infty}^{\infty} \tilde{D}_i(\delta_c - \tau)\tilde{P}_j(\tau)d\tau \qquad (1.47) \\ C_{i,j} &= \int_{Z_i^{\text{start}}}^{Z_i^{\text{end}}} D_i(z)P_j(z)dz \\ &= \tilde{D}_i(z) \star \tilde{P}_j(z) \mid_{z=\delta_r} = \int_{-\infty}^{\infty} \tilde{D}_i(\delta_r - z)\tilde{P}_j(z)dz \qquad (1.48) \end{aligned}$$

where we use $t$ to represent the tangential direction of the detector corresponding to the $i$-th projection, and $z$ to represent the $z$-direction, and denoted $[T_i^{\text{start}}, T_i^{\text{end}}]$ and $[Z_i^{\text{start}}, Z_i^{\text{end}}]$ be the two ends of the detector corresponding to the $i$-th projection, in $t$- and $z$-direction respectively, and $\delta_c$ and $\delta_r$ are the difference between the projection of the center of pixel and the center of the detector in $t$- (channel) and $z$- (row) direction.

It would be very computation demanding if we use the brute force approach to trace every rays from the source to the detectors in order to compute the pixel profile. Instead, we adopt the distance-driven approach [3]. where we flatten each pixel to the plane that is most parallel to the detector plane and model the pixel profile as a rectangular function, which is non-zero along the projection of the center pixel line on the detector plane. We also assume that the detector sensitivity is the rectangular function. As a result, the coefficients $B_{i,j}$ and $C_{i,j}$ will both be the convolution of two rectangular functions, given by

$$\begin{aligned} B_{i,j} &= \frac{\Delta_{xy}}{\cos\tilde{\theta}}\text{rect}\left(\frac{W_c}{2}\right) \star \frac{1}{\Delta d_c}\text{rect}\left(\frac{\Delta d_c}{2}\right) \mid_{t=\delta_c} \qquad (1.49) \\ C_{i,j} &= \frac{\Delta_z}{\cos\phi}\text{rect}\left(\frac{W_r}{2}\right) \star \frac{1}{\Delta d_r}\text{rect}\left(\frac{\Delta d_r}{2}\right) \mid_{z=\delta_r} \qquad (1.50) \end{aligned}$$

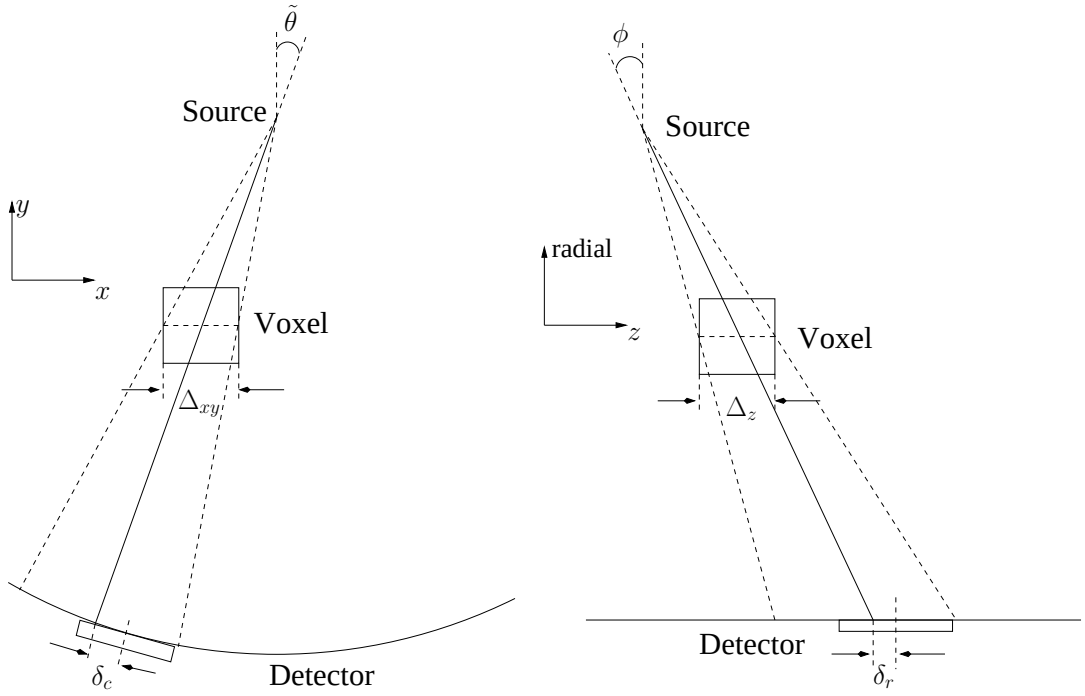


(a) $XY$-plane (b) $Z$ direction

Fig. 1.3.: 3D geometry of multi-slice helical CT

where $W_c$ and $W_r$ are the pixel projection width on $xy$-plane (channel) and $z$-direction (row) respectively. Furthermore, we can further simplify the convolution of two rectangular functions as a series of clipping operation using

$$\text{rect}\left(\frac{a}{2}\right) \star \text{rect}\left(\frac{b}{2}\right) \; |_{t=\delta} = \text{clip}(0, \frac{a+b}{2} - |\delta|, \min(a,b)) \tag{1.51}$$

where we define $\text{clip}(a,b,c) = \min(\max(a,b),c)$. Therefore, we finally get the explicit expression for 3D forward projection coefficient as

$$A_{i,j} = B_{i,j} \times C_{i,j} \tag{1.52}$$

$$B_{i,j} = \frac{\Delta_{xy}}{\Delta d_c \cos\tilde{\theta}} \text{clip}\left(0, \frac{W_c + \Delta d_c}{2} - |\delta_c|, \min\left(W_c, \Delta d_c\right)\right) \tag{1.53}$$

$$C_{i,j} = \frac{1}{\Delta d_r \cos\phi} \text{clip}\left(0, \frac{W_r + \Delta_r}{2} - |\delta_r|, \min\left(W_r, \Delta d_r\right)\right) \tag{1.54}$$

Here the $\theta$ is the adjusted view angle, given by

$$\tilde{\theta} = \left(\theta + \frac{\pi}{4}\right) \mod \frac{\pi}{2} - \frac{\pi}{4} \, . \tag{1.55}$$

## 1.5 Image Prior Model

We model the image prior distribution as a Markov random fields (MRF) [4], which constrains the pixel interactions on a local scale. The probability density of a MRF can be written as a Gibbs distribution,

$$\mathbb{P}(x) = \frac{1}{Z} \exp\left\{ -\sum_{c \in \mathcal{C}} V_c(x_c) \right\} \tag{1.56}$$

where $\mathcal{C}$ denotes the set of all cliques in the image grid, $x_c$ is the subset of pixel values in clique $c$, and $Z$ is the normalization constant known as the partition function, such that

$$Z = \int \exp\left\{ -\sum_{c \in \mathcal{C}} V_c(x_c) \right\} dx \ . \tag{1.57}$$

If we consider only pairwise cliques, the distribution can be simplified as

$$\mathbb{P}(x) = \frac{1}{Z} \exp\left\{ -\sum_{\{s,r\} \in \mathcal{C}} b_{s,r} \tilde{\rho}(x_s, x_r) \right\} \tag{1.58}$$

where $b_{s,r}$ is the weight for pixel $s$ and $r$, and $\tilde{\rho}$ is a positive function known as the potential function. Note that the weight $b_{s,r}$ must be symmetric such as $b_{s,r} = b_{r,s}$ because pixel $s$ and $r$ are un-ordered in the Gibbs distribution. A particular family of potential functions are the one that depends on the pixel difference. As a result, the distribution can be simplified as

$$\mathbb{P}(x) = \frac{1}{Z} \exp\left\{ -\sum_{\{s,r\} \in \mathcal{C}} b_{s,r} \rho\left( \frac{x_s - x_r}{\sigma_x} \right) \right\} \tag{1.59}$$

where $\rho$ is the positive symmetric potential function on the pixel difference and $\sigma_x$ is the scaling parameter which controls the regularization strength.

We consider a specific image prior, which is the q-Generalized Gaussian MRF (q-GGMRF), and its potential function $\rho(\cdot)$ is given by

$$\rho(\Delta) = \frac{|\Delta|^q}{q} \left( \frac{|\Delta/c|^{p-q}}{1 + |\Delta/c|^{p-q}} \right) \tag{1.60}$$

where $1 \leq q \leq p \leq 2$ and $c$ is the parameter to control the regularization behaviors of low and high contrast regions. The q-GGMRF allows more degrees of freedom to control both low-contrast and high-contrast edge characteristics, with the approximate behavior,

$$\rho(\Delta) \approx \begin{cases} \frac{|\Delta|^p}{qc^{p-q}} & |\Delta| \ll c \\ \frac{|\Delta|^q}{q} & |\Delta| \gg c \end{cases} . \tag{1.61}$$

Therefore, when the pixel difference $\Delta$ is very small, the potential is approximately a $p$-norm, while $\Delta$ is very larger, it is approximately a $q$-norm.

## 1.6 Optimization Method

Substituting the expressions for the log likelihood and log prior, the MAP reconstruction (1.2) can be written as the following optimization,

$$\hat{x} = \arg\min_{x \geq 0} \left\{ \frac{1}{2}\|y - Ax\|_D^2 + \sum_{\{s,r\} \in \mathcal{C}} b_{s,r} \rho\left(\frac{x_s - x_r}{\sigma_x}\right) \right\} \tag{1.62}$$

where that we impose a positivity constraint on the image $x$. Such the optimization is solved by iterative methods.

We solve the overall optimization problem using the iterative coordinate descent (ICD) algorithm [4] in which we scan over all the voxels and sequentially optimize each voxel while fixing the others. In particular, consider the update of $x_s$ while fixing th others. We denote the pixel value before the update as $v$ and after as $u$, then the 1D optimization can be written as

$$x_s \leftarrow \arg\min_{u \geq 0} \left\{ \frac{1}{2}\|y - Ax - A_{*,s}(u - v)\|_D^2 + \sum_{\{s,r\} \in \mathcal{C}} b_{s,r} \rho\left(\frac{u - x_r}{\sigma_x}\right) \right\} . \tag{1.63}$$

Notice that the solution to (1.63) does not have a closed form solution due to the complex form of the q-GGMRF potential function. Instead, we use the substitute function minimization method, in which $\rho(\Delta)$ is replaced with an upper bound function $q$ of $\Delta$ and is easier to optimize. It can be shown that if the following properties

of $q$ are satisfied, an update of the modified objective function will also decrease the original function,

$$\rho(\Delta) \leq q(\Delta;\Delta') \tag{1.64}$$

$$\rho(\Delta) = q(\Delta';\Delta') \tag{1.65}$$

where $q(\Delta;\Delta')$ is parametrized by the value $\Delta'$ before the image update. Replacing the original objective function with $q$, we obtain the modified optimization problem

$$x_s \leftarrow \arg\min_{u\geq 0}\left\{\frac{1}{2}\|y-Ax-A_{*,s}(u-v)\|_D^2 + \sum_{\{s,r\}\in\mathcal{C}} b_{s,r}q\left(\frac{u-x_r}{\sigma_x};\frac{v-x_r}{\sigma_x}\right)\right\} . \tag{1.66}$$

If we keep track of the error sinogram $\varepsilon = y - Ax$ and update it after each pixel update, the optimization can be further simplified as

$$v \leftarrow x_s \tag{1.67}$$

$$x_s \leftarrow \arg\min_{u\geq 0}\left\{\theta_1(u-v)+\frac{1}{2}\theta_2(u-v)^2+\sum_{r\in\partial s} b_{s,r}q\left(\frac{u-x_r}{\sigma_x},\frac{v-x_r}{\sigma_x}\right)\right\} \tag{1.68}$$

$$\varepsilon \leftarrow \varepsilon - A_{*,s}(x_s - v) \tag{1.69}$$

where we define the first and second derivatives given by

$$\theta_1 = -A_{*,s}^T D\varepsilon , \tag{1.70}$$

$$\theta_2 = A_{*,s}^T D A_{*,s} . \tag{1.71}$$

We now develop an upper bound of q-GGMRF potential function using the symmetric bound condition. If we define $\Delta = \frac{u-x_r}{\sigma_x}$ and $\Delta' = \frac{v-x_r}{\sigma_x}$, then the substitute function for $\rho(\Delta)$ is given by

$$q(\Delta;\Delta') = \frac{\rho'(\Delta')}{2\Delta'}\Delta^2 \tag{1.72}$$

where

$$\rho'(\Delta') = \frac{|\Delta|^{p-1}}{qc^{p-q}(1+|\Delta/c|^{p-q})}\left(p - \frac{(p-q)|\Delta/c|^{p-q}}{1+|\Delta/c|^{p-q}}\right)\text{sign}(\Delta) . \tag{1.73}$$

This gives the upper bound as

$$q(\Delta;\Delta') = \frac{\rho'(\Delta')}{2\Delta'}\Delta^2 \tag{1.74}$$

$$= \frac{|\Delta'|^{p-2}}{qc^{p-q}(1+|\Delta'/c|^{p-q})}\left(p-\frac{(p-q)|\Delta'/c|^{p-q}}{1+|\Delta'/c|^{p-q}}\right)\Delta^2 \tag{1.75}$$

Substituting the upper bound and setting the derivative of the objective function to zero, we can finally get the closed form solution given by

$$x_s \leftarrow \max\left(0, \frac{-\theta_1+\theta_2 v+\frac{1}{\sigma^2}\sum_{r\in\partial s}\frac{x_r b_{s,r}\rho'\left(\frac{v-x_r}{\sigma}\right)}{\left(\frac{v-x_r}{\sigma}\right)}}{\theta_2+\frac{1}{\sigma^2}\sum_{r\in\partial s} b_{s,r}\frac{\rho'\left(\frac{v-x_r}{\sigma}\right)}{\left(\frac{v-x_r}{\sigma}\right)}}\right) . \tag{1.76}$$

## 1.7 Parallel Computing

To utilize multi-core processing and speed up the reconstruction for large image volumes, we implemented a parallelized ICD update scheme. In this scheme, the full image volume is cut into N boxes along the $Z$-direction as shown in Figure 1.4 and each processor is responsible for updating voxels in one box. Different processors are synchronized once they finish the work; therefore, one synchronization is made per full scan. This will assign each processor a fairly large amount of work to do in parallel and workload is roughly balanced for different processors in order to reduce processor waiting time. Also, since the image is stored with the index in $Z$-direction as the fastest-changing variable, the processors update voxels along $Z$-direction first in order to create better cache efficiency. Moreover, the voxels being updated are selected to be far apart so that they do not share the same sinogram entry, and therefore, can be updated independently.

## 1.8 Results

In this study, we used scan data acquired on a medical scanner and provided by the ALERT (Awareness and Localization of Explosives-Related Threats) Center, at Northeastern University, to conduct our experiments. The reconstructed image is of

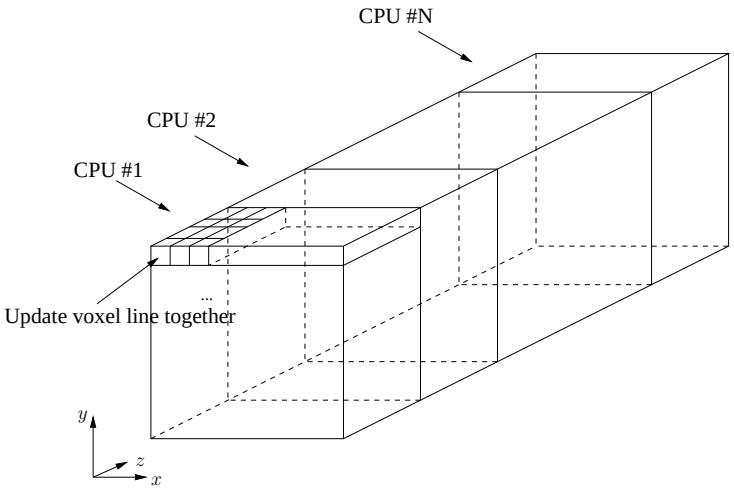


Fig. 1.4.: Parallelized ICD scheme

size $512 \times 512 \times 840$ and the voxel width is 0.975 mm in cross-section in the $XY$-plane and the slice thickness is 1.25 mm in $Z$-direction. Figure 1.5 illustrates some of the objects contained in the bag used in our experiment.

Figure 1.7 demonstrates the quality of different reconstruction algorithms. The FBP reconstruction is blurred, as we can see on the feet of the toy Mr. Potato Head in (a). The shape of some objects are distorted. For example, in the center of (a) and (b), the steel bar, which is of high density and supposed to be a rectangular shape, has been distorted. Also, we can see the severe streaking artifacts, such as the region around the high-density objects in (b). The model-based algorithms, on the other hand, provide better reconstructions. The overall image is sharper and shapes of objects are more accurately recovered. Moreover, the model-based algorithm reduces the structured artifacts as compared to the FBP method. These advantages suggest that the model-based algorithm has the ability to provide more detailed and accurate rendering, which could possibly lead to better detection performance.

We further quantify the reconstruction quality by measuring the noise variance on the uniform region. In Figure 1.6, a target object, which is a plastic bottle of water, is shown. The streaking artifact caused by the nearby high-density metal

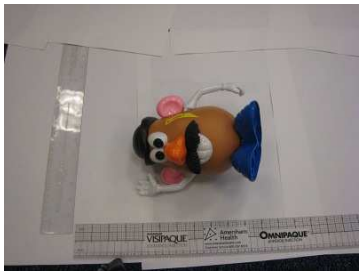

(a)

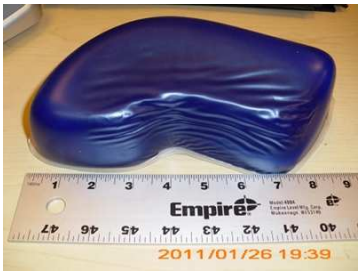


(b)


(c)


(d)

Fig. 1.5.: Objects contained in the baggage (a) toy Mr. Potato Head (b) gel pad (c) steel bar (d) box cutter

object can be easily identified in the FBP reconstruction. We observe that the curve of the FBP reconstruction fluctuates more significantly than the curve of the model-based iterative reconstructions. We further calculate the noise variances with different reconstructions along the line passing through the botter of water vertically and the result is listed in Table 1.1. The FBP reconstruction leads to the largest noise variance, which is the result of the streaking artifacts. It also shows that q-GGMRF gives the smallest noise variance.

Table 1.1: Noise variance on uniform region

| Method | FBP | q-GGMRF |
|---|---|---|
| Noise variance | 3042.8 | 496.5 |

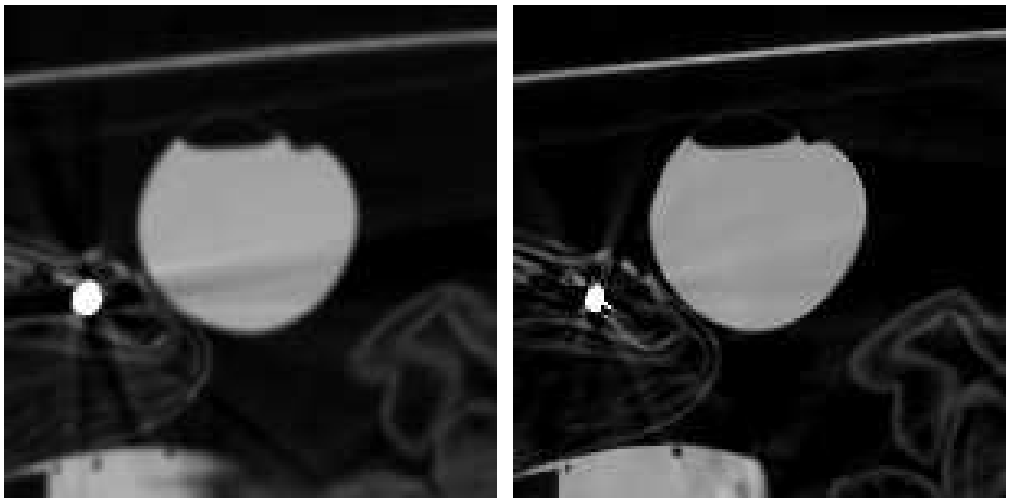

(a) (b)

Fig. 1.6.: Reconstructions zoomed to the target area using (a) FBP, and (b) q-GGMRF The round object is the plastic bottle of water.

## 1.9 Conclusion

In this work, we developed a model-based image reconstruction algorithm and tested it on the data taken from actual baggage. Our algorithm depends on a statistical framework involving a forward model and a prior model. Result shows the model-based algorithms provide better reconstructions and reduce structured artifacts, which suggests potential advantages over the FBP approach.

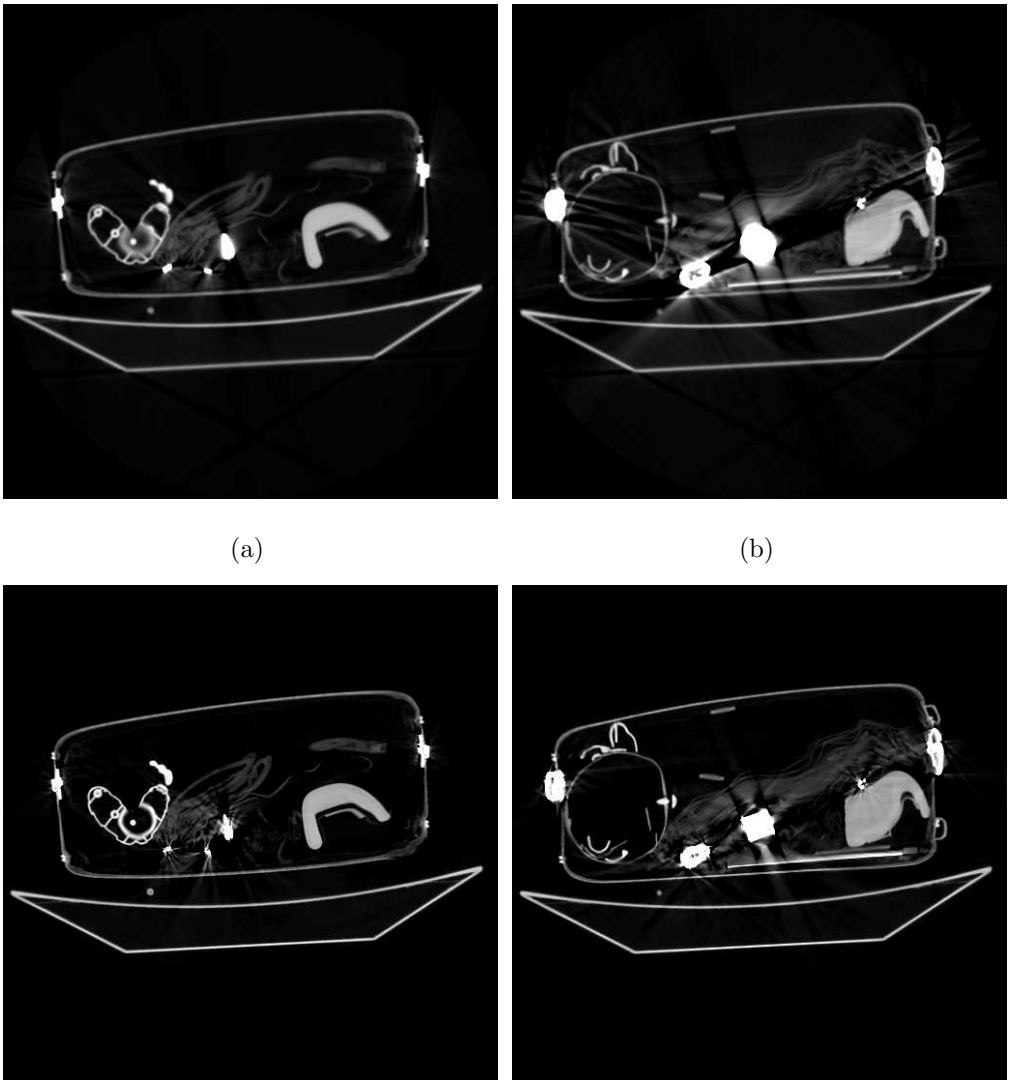

(a) (b)

(c) (d)

Fig. 1.7.: Reconstruction of the ALERT baggage security data using (a, b) FBP, and (c, d) q-GGMRF. The gray scale is in offset Hounsfield Unit (HU), where air = 0 HU and the scale range for all results shown is in $[0, 1600]$ HU.

.

# 2. MODEL-BASED ITERATIVE RECONSTRUCTION WITH SIMULTANEOUS BEAM HARDENING CORRECTION (MBIR-BHC) FOR X-RAY CT

## 2.1 Introduction

X-ray computed tomography (CT) is a widely used imaging modality that depends on the reconstruction of material cross-sections from line integrals of X-ray density. Typically, the required line integrals are obtained by assuming that the X-rays are attenuated exponentially as predicted by Beer-Lambert's law [5]. However, this approximation only holds when the X-ray source is monochromatic. When the X-ray source has a broad spectrum, low-energy photons are typically attenuated more rapidly than high-energy photons; so the beam shifts toward higher energies (i.e., is "hardened") as it passes through the material. The total attenuation is formed by the superposition of weighted exponentials, resulting in the so-called beam-hardening effect [6, 7]. In practice, beam hardening can contribute to cupping and streaking artifacts in the reconstructed images [6–11].

Various algorithms have been proposed to address the beam hardening effect [12–37]. One early approach was to pre-filter the X-ray beam [23] by placing a thin metal plate between the X-ray source and the objects, so as to pre-attenuate the low-energy photons. While such a method is able to narrow the X-ray spectrum and, therefore, reduce the beam hardening effect, it also lowers the detected signal to noise ratio (SNR). Another approach is dual energy scanning [15, 16]. These methods work by reconstructing two material-independent density maps from low and high-energy X-ray measurements. While this technique can fully account for beam-hardening, it requires two spectrally district projection measurements, which is generally much more complex and expensive.

Algorithmic correction is perhaps the most common approach to beam-hardening correction. One widely-used algorithmic correction is linearization, or polynomial pre-correction [6, 12–14]. Pre-correction techniques are based on the assumption that the object is made from a single material, such as water. However, when multiple materials are present, it is not possible to fully compensate for the beam hardening distortion using a single pre-correction function. Alternatively, iterative post-processing techniques are also widely used when the object being scanned is composed of two known materials that can be easily segmented [17–21]. These methods correct the sinogram using knowledge of the two materials' mass attenuation functions, the X-ray source spectrum, and an approximate spatial segmentation into the two materials. In medical imaging applications, it may be reasonable to assume that the object being scanned can be approximately segmented into two known materials, (e.g., soft issue and bone) and the X-ray spectrum is known; so these iterative post-processing techniques can be effective [17, 19, 20]. However, in more general CT applications, such as non-destructive evaluation or security scanning, the objects being scanned may be composed of a number of unknown materials. So the assumptions of iterative post-processing algorithms are violated, and the methods are not straightforward to apply.

Recent results in model-based iterative reconstruction (MBIR) have demonstrated its ability to improve the reconstructed image quality [1, 38–41]. MBIR algorithms typically work by first formulating an overall objective function which incorporates statistical models of both the forward acquisition processes and the objects being reconstructed. The resulting objective functions are then minimized using iterative optimization methods. Several methods have also been developed in order to address the problem of beam hardening in the context of iterative reconstruction [26–29]. De Man et. al. [26] proposed an iterative method which incorporated the knowledge of the known X-ray spectrum into the reconstruction process in order to account for the beam hardening effect. Elbakri et. al. [27, 28] developed an iterative reconstruction method based on the idea of material decomposition. The joint beam hardening

correction polynomial for a set of pre-determined basis materials is pre-calculated and tabulated, and is utilized during the iterative reconstruction. Srivastava et. al. [30] and Abella et. al. [34] extended Elbakri's approach. Their strategy is to design functionals with tuning parameters so that it can map the non-linear effect of two materials into one equivalent material. Therefore, only a single material beam hardening correction polynomial is required. However, all these methods require some additional knowledge of the system, such as X-ray spectrum and mass attenuation functions of the basis materials. In an alternative approach, Kyriakou et. al. proposed a method called Empirical Beam Hardening Correction (EBHC), which does not rely on the prior knowledge of the X-ray spectrum or mass attenuation functions [35]. EBHC is based on direct reconstruction of a set of images formed from sinograms corresponding to the low and high-density components of the image. This set of reconstructions are combined in a way that maximizes flatness of the final corrected image.

In this paper, we propose a novel model-based iterative reconstruction algorithm including correction of beam hardening effects (MBIR-BHC). A preliminary study of this method was presented in conference paper [42, 43]. Unlike most previous methods, which require additional system information in advance, MBIR-BHC works by simultaneously reconstructing the image and estimating the beam hardening correction function. The method is based on the assumption that the object is formed by a combination of two distinct materials that can be separated according to their densities. We formulate a poly-energetic X-ray forward model using a polynomial function of two material projections: one for the low density material and one for the high. We then develop an effective alternating optimization algorithm for estimating the reconstructed image, the material segmentation, and the coefficients of the two component polynomial. Since the correction polynomial and materials segmentation mask are both estimated during the reconstruction process, no additional system information is needed and the correction is automatically adapted to the dataset being reconstructed.

We evaluate the proposed MBIR-BHC algorithm using both simulated and real X-ray CT datasets, including high and low density objects. The experimental results show that the MBIR-BHC algorithm significantly reduces several reconstruction artifacts and improves the overall image quality.

The paper is organized as follows. Section 2.2 presents the poly-energetic X-ray model and formulates the problem of joint reconstruction and correction. Section 2.3 describes the alternating optimization. Section 2.4 shows the experimental results on the simulated and real data to demonstrate the improvement achieved by MBIR-BHC as compared to traditional methods. Finally, Section 2.5 concludes the discussion.

## 2.2 Poly-energetic X-ray Model and Statistical Approach for Reconstruction

### 2.2.1 Poly-energetic Model for X-ray CT

Let $\mu(\mathcal{E}) \in \mathbb{R}^N$ be the vector whose the $j$-th entry $\mu_j(\mathcal{E})$ is the energy-dependent linear attenuation coefficient of the $j$-th pixel. The received photon intensity of the $i$-th projection, denoted by $\lambda_i$, can be modeled as a Poisson random variable with the mean given by

$$\mathbb{E}[\lambda_i|\mu(\mathcal{E})] = \int_{\mathbb{R}} S_i(\mathcal{E}) e^{-\sum_j A_{i,j}\mu_j(\mathcal{E})} d\mathcal{E} \tag{2.1}$$

where $S_i(\mathcal{E})$ is the source-detector energy spectrum, and $A$ is the system forward projection matrix whose entries represent the contribution of the $i$-th projection to the $j$-th pixel. For each projection, the standard CT projection measurement $Y_i$ is generated by

$$Y_i = -\log \frac{\lambda_i}{\lambda_{T,i}} \tag{2.2}$$

where $\lambda_{T,i}$ is the expected photon intensity in an air-calibration scan for the $i$-th projection, given by

$$\lambda_{T,i} = \int_{\mathbb{R}} S_i(\mathcal{E}) d\mathcal{E} \ . \tag{2.3}$$

Denote the normalized energy spectrum as $\tilde{S}_i$ given by

$$\tilde{S}_i(\mathcal{E}) = \frac{S_i(\mathcal{E})}{\lambda_{T,i}} \ . \tag{2.4}$$

We will assume that $\tilde{S}_i(\mathcal{E})$ is the same for all the projections; so the projection index $i$ can be dropped in $\tilde{S}_i$. Putting (2.1) through (2.4), the expected projection measurement can be approximated as

$$\begin{aligned} \mathbb{E}[Y_i|\mu(\mathcal{E})] &\cong -\log\left(\mathbb{E}\left[\frac{\lambda_i}{\lambda_{T,i}}\right]\right) \\ &= -\log\left(\int_{\mathbb{R}} \tilde{S}(\mathcal{E}) e^{-\sum_j A_{i,j}\mu_j(\mathcal{E})} d\mathcal{E}\right) \ . \end{aligned} \tag{2.5}$$

So (2.5) is the conventional model for the non-linear beam hardening that results from a poly-energetic X-ray beam.

Our objective will be to formulate a simple parametric model of the beam-hardening that occurs with a single, polychromatic scan of an object composed of two distinct materials, one with high density and the other with low. To do this, we first define $x_j$ to be the weighted average of the linear attenuation coefficient of the $j$-th pixel with respect to the energy spectrum

$$x_j \triangleq \int_{\mathbb{R}} \tilde{S}(\mathcal{E})\mu_j(\mathcal{E}) d\mathcal{E} \tag{2.6}$$

Using this definition, we can rewrite the energy-dependent linear attenuation coefficient of the $j$-th pixel as

$$\mu_j(\mathcal{E}) = x_j r_j(\mathcal{E}) \tag{2.7}$$

where $r_j(\mathcal{E})$ is the absorption spectrum of the $j$-th pixel, given by

$$r_j(\mathcal{E}) = \frac{\mu_j(\mathcal{E})}{x_j} = \frac{\mu_j(\mathcal{E})}{\int_{\mathbb{R}} \tilde{S}(\mathcal{E})\mu_j(\mathcal{E}) d\mathcal{E}} \ . \tag{2.8}$$

Notice that in this formulation, $r_j(\mathcal{E})$ carries the energy dependency and $x_j$ only depends on the pixel location $j$. Moreover, from (2.8) we see that the weighted energy spectrum of $r_j(\mathcal{E})$ is normalized to 1; so for all $j$,

$$\int_{\mathbb{R}} \tilde{S}(\mathcal{E}) r_j(\mathcal{E}) d\mathcal{E} = 1 \ . \tag{2.9}$$

We first consider the simple case when the scanned object only contains one absorptive material denoted by $\mathcal{M}$. The functions $r_j(\mathcal{E})$ are identical for all pixels $j$ and we have

$$\mu_j(\mathcal{E}) = x_j r_{\mathcal{M}}(\mathcal{E}) \tag{2.10}$$

where $r_{\mathcal{M}}(\mathcal{E})$ is the absorption spectra for the material $\mathcal{M}$. Substituting (2.10) into (2.5), we may define the beam hardening function $f_{\mathcal{M}}(p_i)$ given by

$$f_{\mathcal{M}}(p_i) \triangleq -\log\left(\int_{\mathbb{R}} \tilde{S}(\mathcal{E}) e^{-r_{\mathcal{M}}(\mathcal{E})p_i} d\mathcal{E}\right) \tag{2.11}$$

where $p_i$ is the $i$-th projection given by

$$p_i = \sum_j A_{i,j} x_j \ . \tag{2.12}$$

Let $x \in \mathbb{R}^N$ be the vector with entries $x_j$ defined in (2.6). Using this notation, the expected projection measurement is then given by

$$\mathbb{E}[Y_i|x] = f_{\mathcal{M}}(p_i) \ . \tag{2.13}$$

So from (2.13), we see that the expected projection measurement $\mathbb{E}[Y_i|x]$ will be a nonlinear function $f_{\mathcal{M}}$ of the projection $p_i$. Differentiating (2.11), we show in Appendix 2.6 that

$$\frac{d}{dp_i} f_{\mathcal{M}}(p_i)\Big|_{p_i=0} = 1 \ , \tag{2.14}$$

and therefore, we also know that

$$\frac{d}{dy_i} f_{\mathcal{M}}^{-1}(y_i)\Big|_{y_i=0} = 1 \tag{2.15}$$

where $y_i$ is the dummy variable for the inverse function $f_{\mathcal{M}}^{-1}$. This implies that when the value of the projection is very small (i.e. when the projection passes through a thin soft material), the beam hardening effect is negligible. In practice, since human soft tissue has energy-dependent attenuation similar to water, most current medical systems perform a beam hardening pre-correction with respect to water. More specifically, typical medical imaging systems apply a beam-hardening correction with the

form $f_{\mathcal{M}}^{-1} = f_W^{-1}$, where the subscript $W$ explicitly indicates water as the reference material.

Next consider the case of two materials. In this case, a single correction function can not fully compensate for the effects of beam hardening. In order to better model this case, we will assume the object is made of two distinct materials, one of low density and a second of high density. More formally, we model the absorption spectrum $r_j(\mathcal{E})$ as a convex combination of two distinct absorption spectrum given by

$$r_j(\mathcal{E}) \triangleq (1 - b_j) r_L(\mathcal{E}) + b_j r_H(\mathcal{E}) \ , \tag{2.16}$$

where $r_L(\mathcal{E})$ and $r_H(\mathcal{E})$ represent the absorption spectrum of the "low" and "high" density materials respectively, and $b_j$ represents the fraction of material that is of high density for the $j$-th pixel. Using this model, the linear attenuation coefficient of the $j$-th pixel can be written as

$$\mu_j(\mathcal{E}) = x_j \left( (1 - b_j) r_L(\mathcal{E}) + b_j r_H(\mathcal{E}) \right) \ . \tag{2.17}$$

In this work, we consider only the case in which $b_j$ is binary, i.e. $b_j \in \{0, 1\}$; so each pixel will be composed entirely of either low or high density materials. In order to determine the values of $b_j$, we will estimate them directly from the CT data as part of the reconstruction process. While more discrete classes could be used, this simple two-material decomposition model strikes a balance between accuracy and model simplicity.

Substituting (2.17) into (2.5), we obtain

$$\mathbb{E}[Y_i | x] = h(p_{L,i}, p_{H,i}) \tag{2.18}$$

where $h(p_{L,i}, p_{H,i})$ is now a two dimensional beam hardening function given by

$$h(p_{L,i}, p_{H,i}) \triangleq -\log \left( \int_{\mathbb{R}} \tilde{S}(\mathcal{E}) e^{-r_L(\mathcal{E}) p_{L,i} - r_H(\mathcal{E}) p_{H,i}} d\mathcal{E} \right) \tag{2.19}$$

and $p_{L,i}$ and $p_{H,i}$ are now the projections of the low and high density materials given by

$$p_{L,i} = \sum_j A_{i,j} x_j (1 - b_j) \ , \tag{2.20}$$

$$p_{H,i} = \sum_j A_{i,j} x_j b_j \ . \tag{2.21}$$

So from (2.18), we see that with two materials, the expected projection measurement is now a non-linear function of the two dimensional projections of the two materials. Our approach will be to adaptively estimate this 2D beam hardening function during the reconstruction process. To do this, we adopt a simple polynomial parametrization of the function given by

$$h(p_{L,i}, p_{H,i}) = \sum_{k=0}^{\infty} \sum_{l=0}^{\infty} \gamma_{k,l} (p_{L,i})^k (p_{H,i})^l, \tag{2.22}$$

where $\gamma_{k,l}$ are coefficients to be jointly estimated during the reconstruction.

In fact, some of the coefficients in (2.22) are determined by the physics; so this will simplify our problem. More specifically, if both the projections $p_{L,i}$ and $p_{H,i}$ are 0, plugging them into (2.19), we see that

$$\gamma_{0,0} = h(0,0) = -\log \left( \int_{\mathbb{R}} \tilde{S}(\mathcal{E}) e^0 d\mathcal{E} \right) = 0 \ . \tag{2.23}$$

Also differentiating (2.19) with respect to $p_{L,i}$ and $p_{H,i}$, we obtain in Appendix 2.6 the following two relationships

$$\gamma_{1,0} = \frac{\partial}{\partial p_{L,i}} h(p_{L,i}, 0) \Big|_{p_{L,i}=0} = 1 \ , \tag{2.24}$$

$$\gamma_{0,1} = \frac{\partial}{\partial p_{H,i}} h(0, p_{H,i}) \Big|_{p_{H,i}=0} = 1 \ . \tag{2.25}$$

Table 2.1 lists the coefficients of the function $h$. We will refer to an $p$-th order model as one that includes all the unknown coefficients for $0 \leq k + l \leq p$.

This two-material beam-hardening model can also be used in the case when the projection measurement is pre-corrected for beam hardening of a single material. To see this, suppose the projection measurements have been pre-corrected with respect

Table 2.1: the coefficients of the beam hardening function $h$ used for un-corrected data

| | $l=0$ | $l=1$ | $l=2$ | $l=3$ | $\cdots$ |
|---|---|---|---|---|---|
| $k=0$ | 0 | 1 | $\gamma_{0,2}$ | $\gamma_{0,3}$ | $\cdots$ |
| $k=1$ | 1 | $\gamma_{1,1}$ | $\gamma_{1,2}$ | $\gamma_{1,3}$ | $\cdots$ |
| $k=2$ | $\gamma_{2,0}$ | $\gamma_{2,1}$ | $\gamma_{2,2}$ | $\gamma_{2,3}$ | $\cdots$ |
| $k=3$ | $\gamma_{3,0}$ | $\vdots$ | $\vdots$ | $\vdots$ | $\ddots$ |

to the material $\mathcal{M}$ using the function $f_{\mathcal{M}}^{-1}$. As a result, the expected projection measurement, after pre-correction, is approximately given by

$$\mathbb{E}[Y_i|x] = \tilde{h}(p_{L,i}, p_{H,i}) \tag{2.26}$$

where the 2D beam hardening function $\tilde{h}$ is now given by

$$\tilde{h}(p_{L,i}, p_{H,i}) \triangleq f_{\mathcal{M}}^{-1}\left(-\log\left(\int_{\mathbb{R}} \tilde{S}(\mathcal{E}) e^{-r_L(\mathcal{E})p_{L,i} - r_H(\mathcal{E})p_{H,i}} d\mathcal{E}\right)\right) \ . \tag{2.27}$$

Using the similar approach as in (2.22), we can parametrize $\tilde{h}$ using a high-order polynomial as

$$\tilde{h}(p_{L,i}, p_{H,i}) = \sum_{k=0}^{\infty}\sum_{l=0}^{\infty} \tilde{\gamma}_{k,l} (p_{L,i})^k (p_{H,i})^l \tag{2.28}$$

where $\tilde{\gamma}_{k,l}$ are the polynomial coefficients. Moreover, we show in Appendix 2.6 that in this case similar constraints hold with

$$\tilde{\gamma}_{0,0} = \tilde{h}(0,0) = 0 \ , \tag{2.29}$$

$$\tilde{\gamma}_{1,0} = \frac{\partial}{\partial p_{L,i}} \tilde{h}(p_{L,i}, 0)\Big|_{p_{L,i}=0} = 1 \ , \tag{2.30}$$

$$\tilde{\gamma}_{0,1} = \frac{\partial}{\partial p_{H,i}} \tilde{h}(0, p_{H,i})\Big|_{p_{H,i}=0} = 1 \ . \tag{2.31}$$

In practice, it is common to pre-correct the projection measurements, $Y_i$, for the beam hardening due to the low-density material. In medical applications, this correction

Table 2.2: the coefficients of the beam hardening function $\tilde{h}$ used for pre-corrected data

| | $l=0$ | $l=1$ | $l=2$ | $l=3$ | $\cdots$ |
|---|---|---|---|---|---|
| $k=0$ | 0 | 1 | $\tilde{\gamma}_{0,2}$ | $\tilde{\gamma}_{0,3}$ | $\cdots$ |
| $k=1$ | 1 | $\tilde{\gamma}_{1,1}$ | $\tilde{\gamma}_{1,2}$ | $\tilde{\gamma}_{1,3}$ | $\cdots$ |
| $k=2$ | 0 | $\tilde{\gamma}_{2,1}$ | $\tilde{\gamma}_{2,2}$ | $\tilde{\gamma}_{2,3}$ | $\cdots$ |
| $k=3$ | 0 | $\vdots$ | $\vdots$ | $\vdots$ | $\ddots$ |

is usually based on a water phantom since human soft tissue is largely composed of water. In this case, the pre-correction is given by $f_{\mathcal{M}}^{-1} = f_L^{-1}$ where $f_L^{-1}$ is the ideal beam-hardening correction for the low density material. By definition, we know that this pre-correction will linearize the low density measurement so that

$$\tilde{h}(p_{L,i}, 0) = f_L^{-1}(f_L(p_{L,i})) = p_{L,i} \ . \tag{2.32}$$

This implies that $\tilde{\gamma}_{k,0} = 0$ for $k \neq 1$. Table 2.2 lists the coefficients of the function $\tilde{h}$.

In summary, we have shown that the two-material beam-hardening model can be used for both pre-corrected and un-corrected projection data. In both cases, the three coefficients $\gamma_{0,0} = 0$ and $\gamma_{0,1} = \gamma_{1,0} = 1$ are pre-determined. Depending on the selected model order, the set of remaining coefficients are then estimated as part of the reconstruction algorithm. In particular, for a 2-nd order model ($p = 2$), the unknown coefficients to be estimated are $\gamma_{k,l}$ for $(k,l) \in \{(1,1),(0,2)\}$; and for a 3-rd order model ($p = 3$), then the unknown coefficients to be estimated are $\gamma_{k,l}$ for $(k,l) \in \{(1,1),(2,1),(0,2),(1,2),(0,3)\}$.

As a final remark, we will use the unified notation $h(\cdot,\cdot)$ and $\gamma_{k,l}$ to denote the correction polynomial and its coefficients throughout the following discussion This is only

to keep our notation simple. We will explicitly state the pre-correction information and the polynomial order we use when we present the experiment results.

### 2.2.2 Statistical Model and Objective Function

Let $x \in \mathbb{R}^N$ be the image vector, $y \in \mathbb{R}^M$ be the vector of the projection measurements, $b \in \{0,1\}^N$ be the vector of the material segmentation label mask, and $\gamma \in \mathbb{R}^K$ be the vector of the fitting coefficients $\gamma_{k,l}$. So $K = 2$ if the 2-nd order model in Table 2.2 is used and $K = 5$ if the 3-rd order model is used, etc. We treat $\gamma$ as the nuisance parameter and formulate the problem of simultaneous image reconstruction and beam hardening correction as the computation of the maximum a posterior (MAP) estimate given by

$$\{\hat{x}, \hat{b}, \hat{\gamma}\} = \underset{x \geq 0, b, \gamma}{\arg\min} \{-\log \mathbb{P}(y|x, b, \gamma) - \log \mathbb{P}(x, b)\} \tag{2.33}$$

where $\mathbb{P}(y|x, b, \gamma)$ is the likelihood function corresponding to the X-ray forward model, and $\mathbb{P}(x, b)$ is the joint prior distribution over the image $x$ and the material segmentation mask $b$. Note that we require the image to be non-negative. The parameter vector $\gamma$ is adaptively estimated in this framework. Such an approach has been studied previously in [44] and one may interpret it as computation of the joint maximum *a posteriori* (MAP) and maximum likelihood (ML) estimates of the unknown variables and the nuisance parameters, respectively.

Assuming the projection measurements $Y_i$ are conditionally independent with mean given by (2.19), the negative log likelihood function can be written, within a constant, as

$$-\log \mathbb{P}(y|x, b, \gamma) \approx \frac{1}{2} \sum_{i=1}^{M} w_i (y_i - h(p_i))^2 \tag{2.34}$$

where $p_i = [p_{L,i}\ p_{H,i}]^T$, and $w_i$ is the statistical weight for the $i$-th projection, which is approximately proportional to the inverse of variance of the measurement $Y_i$. Note that taking the log of the signal in equation (2.19) can cause a slight mean shift in

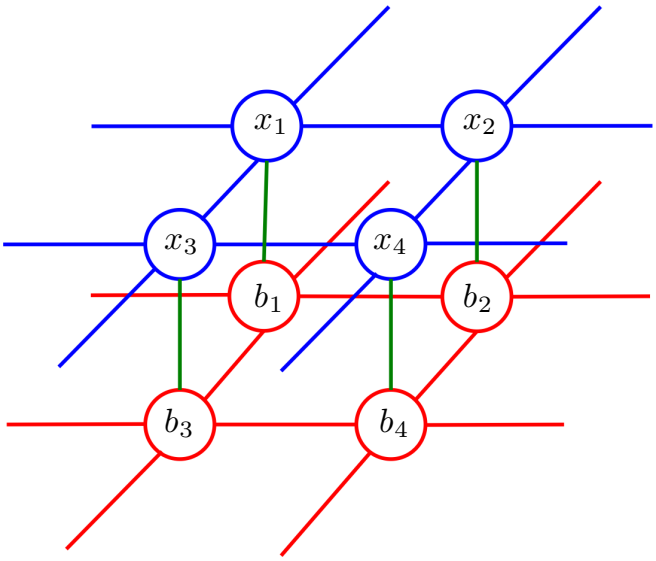


Fig. 2.1.: Illustration of the joint prior over $x$ and $b$ as a two-layer MRF. Pixels $x_j$ are connected through the blue potentials $\rho$. Material segmentation labels $b_j$ are connected through the red potentials $\phi$. Pixels and segmentation labels are also connected through the green potentials $\psi$.

the signal since the log is concave. However, for the purposes of this paper, we will assume that means shift is negligible.

Using this assumption, $w_i$ can also be computed approximately as

$$w_i = \frac{\lambda_i^2}{\lambda_i + \sigma_e^2} \tag{2.35}$$

where $\sigma_e^2$ is the variance of the additive electronic noise.

To model the joint prior over $x$ and $b$, we adopt the Markov random field (MRF) model. We want to model not only the interactions among pixels or segmentation labels themselves, but also the interactions between pixels and segmentation labels. Our model is a two-layer pairwise MRF, one for the image $x$ and the other for the material segmentation mask $b$. Nodes on one layer connect to their corresponding counterparts on the other. Figure 2.1 illustrates this graphical model. From this

structure, we may write the joint prior distribution over $x$ and $b$ as

$$\mathbb{P}(x,b) = \frac{1}{Z}\exp\left\{ -\sum_{\{j,k\}\in\mathcal{C}} \alpha_{j,k}\rho(x_j,x_k) - \beta\sum_{j=1}^{N}\psi(x_j,b_j) - \sum_{\{j,k\}\in\mathcal{C}} \eta_{j,k}\phi(b_j,b_k)\right\} \quad (2.36)$$

where $\mathcal{C}$ denotes the set of all pairwise cliques, $\rho$, $\psi$ and $\phi$ are the positive potential functions on $x$, $b$, and the interactions between them, respectively, and $Z$ denotes the partition function making the whole function a valid probability distribution. The parameters $\alpha_{j,k}$, $\beta$ and $\eta_{j,k}$ are the corresponding weights for edges in the graph. We choose $\alpha_{j,k}$ and $\eta_{j,k}$ to be inversely proportional to the distance between pixel $j$ and $k$. Moreover, the scales of these parameters are empirically adjusted to balance among noise, resolution and segmentation error in the final reconstruction. We have listed the selected parameters for each dataset we test in the Result section.

For the pixel pairwise potential $\rho$, we use the q-generalized Gaussian MRF (q-GGMRF) potential function [1], given by

$$\rho(x_j,x_k) \triangleq \frac{|x_j - x_k|^p}{1 + |(x_j - x_k)/c|^{p-q}} \quad (2.37)$$

where $1 \le q \le p = 2$. Notice that the function only depends on the pixel difference $\Delta = x_j - x_k$ and a pair of pixels with small difference results high probability. Here $c$ is a tuning parameter to balance the performance between noise reduction and edge preservation. If $|\Delta| \ll c$, $\rho(\Delta) \approx |\Delta|^p$ and if $|\Delta| \gg c$, $\rho(\Delta) \approx |\Delta/c|^q$.

The potential $\psi$, which captures the inter-layer interactions, should be chosen such that it gives high probabilities if the segmentation label correctly reflects the pixel value and gives low probabilities otherwise. We design the potential $\psi$ to be

$$\psi(x_j,b_j) \triangleq (x_j - T)_+(1 - b_j) + (T - x_j)_+ b_j \quad (2.38)$$

where $(x)_+ = \max\{x, 0\}$ and $T$ is the user-defined threshold. This is a linear loss function which penalizes the mismatch of the pixel and its corresponding segmentation label. Specifically, when $b_j = 0$, indicating that the pixel belongs to the low density material, $\psi$ will impose a linear penalty if $x_j$ exceeds the attenuation threshold $T$. Symmetrically, a linear penalty will be imposed in the case when $x_j \le T$ and $b_j = 1$.

The potential $\phi$ over the binary segmentation label should encourage the similarity of the neighboring labels. We design it to be

$$\phi(b_j, b_k) \triangleq 1 - \delta(b_j - b_k) \tag{2.39}$$

where $\delta(\cdot)$ is the discrete delta function taking the value 1 at 0 and 0 elsewhere.

Combining the log likelihood term of (2.34) and the two-layer MRF joint prior over $x$ and $b$ in (2.36), we obtain the overall MAP estimation problem as

$$\{\hat{x}, \hat{b}, \hat{\gamma}\} = \arg\min_{x \geq 0, b, \gamma} \left\{ \frac{1}{2} \sum_{i=1}^{M} w_i (y_i - h(p_i))^2 + \sum_{\{j,k\} \in \mathcal{C}} \alpha_{j,k} \rho(x_j - x_k) \right.$$
$$\left. + \beta \sum_{j=1}^{N} ((x_j - T)_+ (1 - b_j) + (T - x_j)_+ b_j) + \sum_{\{j,k\} \in \mathcal{C}} \eta_{j,k} (1 - \delta(b_j - b_k)) \right\} . \tag{2.40}$$

We refer to (2.40) as the objective function in our reconstruction framework.

## 2.3 Iterative Beam Hardening Correction and Image Reconstruction

### 2.3.1 Estimation of the Beam Hardening Correction Polynomial

Fixing $x$ and $b$, we first attack the problem of minimizing the objective function with respect to $\gamma$. This becomes a standard weighted least squares problem given by

$$\hat{\gamma} = \arg\min_{\gamma} \frac{1}{2} \sum_{i=1}^{M} w_i (y_i - h(p_i))^2 = \arg\min_{\gamma} \frac{1}{2} \|y - H\gamma\|_W^2 \tag{2.41}$$

where $H \in \mathbb{R}^{M \times K}$ is a matrix whose columns correspond specific terms in the correction polynomials of all the projections in (2.28) and $W = \text{diag}\{w_1, \cdots, w_M\}$. The solution can then be computed in the closed form as

$$\hat{\gamma} = (H^T W H)^{-1} H^T W y \ . \tag{2.42}$$

### 2.3.2 Image Reconstruction as Optimization

Next, we fix $\gamma$ and $b$ and minimize the objective function (2.40) with respect to $x$. Since $h(p_i)$ is a polynomial function of $p_i$, which is in turn a linear function of $x$,

(2.40) will be a higher order function of $x$, rather than a simple quadratic. Thus, the function (2.40) can be in general difficult to solve.

We approach the optimization by applying the Newton-Raphson technique. More specifically, we replace the original optimization (2.40) over $x$ with the following modified optimization

$$\hat{x} = \arg\min_{x \geq 0} \left\{ \sum_{i=1}^{M} (d^{(i),T}(p_i - \hat{p}_i) + \frac{1}{2}(p_i - \hat{p}_i)^T Q^{(i)}(p_i - \hat{p}_i)) + \sum_{\{j,k\} \in \mathcal{C}} \alpha_{j,k} \rho(x_j - x_k) \right. \\ \left. + \beta \sum_j \left( (x_j - T)_+ (1 - b_j) + (T - x_j)_+ b_j \right) \right\} \quad (2.43)$$

where $d^{(i)} \in \mathbb{R}^2$ and $Q^{(i)} \in \mathbb{R}^{2\times 2}$ are the gradient and Hessian of the function $\frac{1}{2} w_i (y_i - h(p_i))^2$ at the point $\hat{p}_i$, given by

$$d^{(i)} = -w_i (y_i - h(\hat{p}_i)) \nabla h(\hat{p}_i) \ , \quad (2.44)$$

$$Q^{(i)} = w_i \nabla h(\hat{p}_i) \nabla h(\hat{p}_i)^T - w_i (y_i - h(\hat{p}_i) \mathrm{Hess}(h(\hat{p}_i)) \ , \quad (2.45)$$

and $\hat{p}_i$ is the projection vector of the previous estimate of $\hat{x}$. The term $\mathrm{Hess}(h(\hat{p}_i)) \in \mathbb{R}^{2\times 2}$ is given by

$$\mathrm{Hess}(h(\hat{p}_i)) = \left[ \begin{array}{cc} \frac{\partial^2}{\partial p_{L,i}^2} h(p_i) & \frac{\partial^2}{\partial p_{L,i} \partial p_{H,i}} h(p_i) \\ \frac{\partial^2}{\partial p_{L,i} \partial p_{H,i}} h(p_i) & \frac{\partial^2}{\partial p_{H,i}^2} h(p_i) \end{array} \right] \Bigg|_{p_i = \hat{p}_i} . \quad (2.46)$$

By doing this, we essentially reduce (2.40) to (2.43), which is a quadratic function plus the remaining prior terms. The same approach has been used in other non-quadratic optimization problems such as [45, 46]. Such a quadratic approximation is generally not an upper bound, which means convergence of the algorithm is not guaranteed without further innovations. However, this approximation is effective and in practice, as we will show in the Results section, we have empirically observed that the resulting updates consistently reduce the objective function of (2.40). The overall algorithm works by first constructing the quadratic approximation (2.43) using the previous projections $\hat{p}_i$ and optimizing (2.43) to obtain the next estimate of $\hat{x}$. The projections $\hat{p}_i$ are then updated and are used in the next iteration.

There are a number of techniques that can be applied to optimize the quadratic approximation (2.43). We choose the iterative coordinate descent (ICD) algorithm. The ICD algorithm updates each pixel in sequence with the other pixels fixed until convergence. Here we present a sketch of derivations of the pixel update and more detailed derivations can be found in Appendix 2.7. Following the similar strategy in [38], the $j$-th pixel update can be computed by solving the 1D optimization given by

$$x_j = \arg\min_{u \geq 0} \left\{ \theta_1(u - \tilde{x}_j) + \frac{1}{2}\theta_2(u - \tilde{x}_j)^2 + \sum_{k \in \partial j} \alpha'_{j,k}(u - x_k)^2 \right. \\ \left. + \beta \left( (u - T)_+(1 - b_j) + (T - u)_+ b_j \right) \right\} \quad (2.47)$$

where $\tilde{x}_j$ denotes the previous value of the pixel, $\partial j$ represents the set of neighbors of the $j$-th pixel, and the coefficient $\alpha'_{j,k}$ is given by

$$\alpha'_{j,k} = \alpha_{j,k} \frac{\rho'(\tilde{x}_j - x_k)}{2(\tilde{x}_j - x_k)} \ . \quad (2.48)$$

Here $\rho'(\cdot)$ is the first derivative of $\rho(\cdot)$ and $\theta_1$ and $\theta_2$ are the first and second derivatives of the first term in (2.43) with respect to $x_j$, given by

$$\theta_1 = \sum_{i=1}^{M} \left( \left( d^{(i),T} + (p_i - \hat{p}_i)^T Q^{(i)} \right) \begin{bmatrix} A_{i,j}(1 - b_j) \\ A_{i,j} b_j \end{bmatrix} \right) \quad (2.49)$$

$$\theta_2 = \sum_{i=1}^{M} \begin{bmatrix} A_{i,j}(1 - b_j) & A_{i,j} b_j \end{bmatrix} Q^{(i)} \begin{bmatrix} A_{i,j}(1 - b_j) \\ A_{i,j} b_j \end{bmatrix} \ . \quad (2.50)$$

To obtain the optimal solution to (2.47), we define two quantities $D_1$ and $D_2$ as

$$D_1 = \theta_1 - \theta_2 \tilde{x}_j - 2 \sum_{k \in \partial j} \alpha'_{j,k} x_k \ , \quad (2.51)$$

$$D_2 = \theta_2 + 2 \sum_{k \in \partial j} \alpha'_{j,k} \ . \quad (2.52)$$

Using this notation, the optimal update can be obtained by applying a shrinkage operation. More specifically, when $b_j = 0$, we have the update given by

$$x_j \leftarrow \mathcal{S}_{\frac{\beta}{2D_2}} \left( -\frac{D_1}{D_2} - T - \frac{\beta}{2D_2} \right) + T \quad (2.53)$$

where the shrinkage operator is defined as

$$\mathcal{S}_\lambda(z) = \text{sign}(z)\max\{|z| - \lambda, 0\} \ , \tag{2.54}$$

and when $b_j = 1$, we have

$$x_j \leftarrow \mathcal{S}_{\frac{\beta}{2D_2}}\left(-\frac{D_1}{D_2} - T + \frac{\beta}{2D_2}\right) + T \ . \tag{2.55}$$

Having obtained the optimal $x_j$, we then re-allocate the projection using the projection update equation given by

$$\begin{bmatrix} p_{L,i} \\ p_{H,i} \end{bmatrix} \leftarrow \begin{bmatrix} p_{L,i} \\ p_{H,i} \end{bmatrix} + \begin{bmatrix} A_{i,j}(1 - b_j) \\ A_{i,j} b_j \end{bmatrix} (x_j - \tilde{x}_j) \ . \tag{2.56}$$

This will finish the ICD update of one specific pixel. Figure 2.2 summarizes the pseudocode of the ICD update for a specific pixel.

### 2.3.3 Optimization Over the Material Segmentation Mask

The segmentation vector $b$ is initialized by thresholding the initial reconstruction $x^{(\text{init})}$ at the begining of the algorithm, given by

$$b_j = \begin{cases} 0 & \text{if } x_j^{(\text{init})} \leq T \\ 1 & \text{otherwise} \end{cases} \ . \tag{2.57}$$

During the alternating optimization, we fix $x$ and $\gamma$, and find the configuration of $b$ which minimizes the overall objective function (2.40). We use the iterative conditional mode (ICM) algorithm. This requires us to solve the 1D optimization of a particular segmentation label as follows

$$b_j = \underset{t\in\{0,1\}}{\arg\min} \left\{ \frac{1}{2}\sum_{i=1}^{M} w_i (y_i - h(p_i))^2 + \sum_{k\in\partial j} \eta_{j,k}(1 - \delta(t - b_k)) \right. \\ \left. + \beta((x_j - T)_+(1 - t) + (T - x_j)_+ t) \right\} \ . \tag{2.58}$$

```
ICDUpdate { /* ICD update for the j-th pixel */
x̃_j ← x_j
θ_1, θ_2 ← calculate using (2.49) and (2.50)
D_1, D_2 ← calculate using (2.51) and (2.52)
if b_j = 0 then
   x_j ← calculate using (2.53)
   for i = 1 to M do
      p_{L,i} ← p_{L,i} + A_{i,j}(x_j − x̃_j)
   end for
else if b_j = 1 then
   x_j ← calculate using (2.55)
   for i = 1 to M do
      p_{H,i} ← p_{H,i} + A_{i,j}(x_j − x̃_j)
   end for
end if
return x_j
}
```

Fig. 2.2.: Pseudocode of ICD update of the pixel $x_j$. First, we calculate the parameters $\theta_1$, $\theta_2$, $D_1$ and $D_2$. Second, we perform the update procedure according to (2.53) or (2.55) depending on the value of $b_j$. Finally, we update the projection vector using (2.56) and return the pixel update.

The actual implementation is to evaluate the 1D objective function (2.58) for $t = 0$ or 1 and to choose the optimal configuration of $t$ which gives the lower cost. After the label is updated, we adjust the projection according to this optimal configuration.

If we let $\tilde{b}_j$ and $b_j$ be the labels of the pixel before and after the ICM update, the projection update is given by

$$\begin{bmatrix} p_{L,i} \\ p_{H,i} \end{bmatrix} \leftarrow \begin{bmatrix} p_{L,i} \\ p_{H,i} \end{bmatrix} + \begin{bmatrix} \tilde{b}_j - b_j \\ b_j - \tilde{b}_j \end{bmatrix} A_{i,j} x_j \ . \tag{2.59}$$

Figure 2.3 shows the pseudocode of the overall MBIR-BHC algorithm for simultaneous image reconstruction and beam hardening correction, which alternates over the optimization of the polynomial coefficients $\gamma$, the image $x$ and the material segmentation label mask $b$.

## 2.4 Results

In the following section, we evaluate MBIR with beam-hardening correction (MBIR-BHC) using both simulated and real data sets, and we compare it to FBP, generic MBIR with a mono-energetic X-ray model (MBIR-mono), and the Empirical Beam Hardening Correction (EBHC) method [35]. The cost function for MBIR-mono is given by

$$\hat{x} = \arg\min_{x \geq 0} \left\{ \frac{1}{2} \|y - Ax\|_W^2 + \sum_{\{j,k\} \in \mathcal{C}} \alpha_{j,k} \rho(x_j - x_k) \right\} \ ; \tag{2.60}$$

and we use the q-GGMRF potential function (2.37) for $\rho$. Both MBIR-mono and MBIR-BHC use the FBP reconstruction as an initial condition for optimization. Also, the segmentation, $b_j$, is initialized with a thresholded version of the FBP image, and we use a $3 \times 3$ neighborhood with coefficients $\alpha_{j,k}$ and $\eta_{j,k}$ selected so that

$$\alpha_{j,k} = \alpha g_{j,k}, \quad \eta_{j,k} = \eta g_{j,k} \ . \tag{2.61}$$

Here $\alpha$, $\eta$ are two scalars and $g_{j,k}$ are the relative weights for different neighboring pixels, given by the following 2D array of values,

| | | |
|---|---|---|
| 0.11 | 0.14 | 0.11 |
| 0.14 | 0 | 0.14 |
| 0.11 | 0.14 | 0.11 |

Table 2.3: the regularization parameter setting of MBIR-BHC for different experiments

| Experiment | $\alpha$ | $\beta$ | $\eta$ |
|---|---|---|---|
| two-material phantom | 0.382 | 0.024 | 0.024 |
| multi-material phantom (noiseless) | 0.514 | 0.033 | 0.033 |
| multi-material phantom (noisy) | 0.013 | 0.033 | 0.033 |
| modified NCAT phantom | 0.630 | 0.040 | 0.040 |
| real baggage scan | 0.607 | 0.039 | 0.039 |

where the center cell represents the pixel being considered. In Table 2.3, we list the parameters $\alpha$, $\beta$ and $\eta$ that were used for each experiment. For the EBHC method, the basic images are reconstructed using FBP. Unless otherwise stated, all MBIR-BHC results use a 2-nd order model with $p = 2$.

### 2.4.1 Simulation Results

In this section, we study the performance of different methods on various phantoms using the computer-simulated parallel-beam transmission polychromatic X-ray projections. The X-ray source spectrum we use is modelled using SPEC78 software from IPEM Report 78 [47] (tube voltage 95kV, incident mean 56.4093 keV, std 14.2177 keV), and its normalized energy spectrum is plotted in Figure 2.4. Furthermore, in all the following simulation studies, the projections are pre-corrected with respect to water using the standard polynomial fitting technique described in [7]. The resulting pre-corrected projection will be used as the input for the different methods.

Table 2.4: the mean intensity (HU) of the water region in Figure 2.5

| | |
|---|---|
| ground truth | 0 |
| FBP | -5.8 |
| MBIR-mono | -7.5 |
| EBHC | -44.2 |
| 2-nd order MBIR-BHC | -7.2 |
| 3-rd order MBIR-BHC | -7.3 |

**The Two-Material Disk Phantom**

The first phantom we study is a two-material phantom, made of a water disk with two aluminium insertions, as shown in Figure 2.5(a). The radius of the water disk and the aluminium insertions are 90 mm and 10 mm, respectively. The parallel-beam projection sinogram has 1024 detectors with 0.24 mm spacing and 720 projection angles over 180 degrees. We do not simulate the noise and scatter effects. All the reconstructed images are 512×512 over the 250 mm FOV. For MBIR-BHC, both the 2-nd and 3-rd order polynomial model are used and the segmentation threshold $T$ is 800 HU. The reconstruction results using different methods are presented in Figure 2.5(b)-(i). Both FBP and MBIR-mono reconstructions contain streak artifacts due to the aluminium insertions. The EBHC method is able to partially suppress the streaks. However, the dark band connecting two insertions is still noticeable. The MBIR-BHC reduces the streak artifacts more effectively. However, in this case, the 3-rd order MBIR-BHC model seems to provide little benefit relative to the 2-nd order MBIR-BHC model. In Table 2.4, the mean intensity of the water region is listed. Notice that the EBHC tends to introduce a bias in the reconstruction, possibly due to the imperfect water pre-correction.

Table 2.5: Quantitative Comparison of the Modeling Error

| | MBIC-mono | 2-nd MBIR-BHC | 3-rd MBIR-BHC |
|---|---|---|---|
| absolute mean | 0.1187 | 0.1172 | 0.1177 |
| variance | 0.0476 | 0.0436 | 0.0448 |

Using the two-material phantom, we further investigate the modeling error in MBIR-mono and MBIR-BHC method. In particular, we simulate the projection $y_i$ as in (2.27) using Monte Carlo method followed by the water pre-correction, and calculate the modeling error as the difference between $y_i$ and the forward projection of the phantom. Mathematically, the modeling error in MBIR-mono is given by

$$e_i^{(\text{MBIR-mono})} = y_i - \sum_{j=1}^{N} A_{i,j} x_j^{(\text{phantom})}, \tag{2.62}$$

and for MBIR-BHC, it is

$$e_i^{(\text{MBIR-BHC})} = y_i - \sum_{0 \le k+l \le p} \tilde{\gamma}_{k,l} (p_{L,i})^k (p_{H,i})^l \tag{2.63}$$

where $p_{L,i}$ and $p_{H,i}$ are the projections of low and high density materials of $x^{(\text{phantom})}$ and $\tilde{\gamma}_{k,l}$ are the convergent parameters produced by MBIR-BHC. We study the 2-nd order MBIR-BHC ($p = 2$) and 3-rd order MBIR-BHC ($p = 3$). Figure 2.6 compares the modeling error of MBIR-mono and MBIR-BHC. All three methods have visible errors in the trace of high density insertions. Notice that the approximation error by the 2-nd order MBIR-BHC is somewhat smaller than the error for MBIR-mono. However, once again, the 3-rd order MBIR-BHC model is no better than the 2-nd order model. The corresponding quantitative results listed in Table 2.5 also show that the 2-nd order MBIR-BHC gives smaller absolute mean and variance of the approximation error than MBIR-mono.

Table 2.6: chemical composition of various materials used in Figure 2.7(a)

| cylinder # | material | density (g/cc) | chemical formula |
|---|---|---|---|
| 1 | polypropylene | 0.90 | $C_3H_6$ |
| 2 | polystryrene | 1.05 | $C_8H_8$ |
| 3 | acrylic | 1.2 | $C_5H_8O_2$ |
| 4 | ULTEM | 1.32 | $C_{37}H_{24}N_2O_6$ |
| 5 | ETFE | 1.7 | $C_2H_4 + C_2F_4$ |
| 8 | PVC | 1.4 | $C_2H_3Cl$ |

**The Multi-Material Disk Phantom**

We continue the simulation study using a multi-material phantom, which consists of a water disk with radius of 90 mm, with several insertions of radius 10 mm, as shown in Figure 2.7(a). The chemical composition of the numbered objects are listed in Table 2.6.

We first simulate a parallel-beam projection sinogram with 1024 detectors of 0.24 mm and 720 projection angles over 180 degrees. We do not simulate the noise and scatter effects. All the reconstructed images are 512×512 over the 250 mm FOV. For MBIR-BHC, the 2-nd order polynomial model is used and the segmentation threshold $T$ is 800 HU. The reconstruction results using different methods are presented in Figure 2.7. Notice that severe streaks through the high density objects are present in FBP and MBIR-mono reconstructions. In the EBHC reconstruction, streaks are suppressed but there are still noticeable artifacts remaining. In contrast, MBIR-BHC significantly reduces the streak artifacts. A corresponding improvement is also observed in the difference images. Figure 2.8 shows a comparison of the mean reconstructed values of the objects # 1-5 as compared to the theoretically correct values

Table 2.7: values of the polynomial coefficients estimated by MBIR-BHC for the experiment in Figure 2.9

| model | $\tilde{\gamma}_{1,1}$ | $\tilde{\gamma}_{0,2}$ | $\tilde{\gamma}_{2,1}$ | $\tilde{\gamma}_{1,2}$ | $\tilde{\gamma}_{0,3}$ |
|---|---|---|---|---|---|
| 2-nd order | 0.00945 | -0.03231 | 0 | 0 | 0 |
| 3-nd order | 0.03923 | -0.03038 | -0.00731 | -0.00913 | 0.00511 |

obtained from equation (2.6). The three algorithms of FBP, MBIR-mono and MBIR-BHC all produce attenuation coefficients with approximately equal accuracy, while EBHC introduces a bias in the mean reconstructed values.

Using the same simulated data from the multi-material phantom, we further investigate the effect of the order of the polynomial model in MBIR-BHC. Table 2.7 lists the values of the polynomial coefficients estimated by the 2-nd and 3-rd order MBIR-BHC. Figure 2.9 compares the result of 2-nd and 3-rd order models for MBIR-BHC. By visual comparison, the 3-rd order MBIR-BHC reconstruction is slightly better than the 2-nd order result and the subtle improvement can be also noticed in the difference image. However, increasing parameters in higher order models may lead to the over-fitting of the projection data and also requires more computation. In practice, we have found that the 2-nd order MBIR-BHC model is sufficient to provide good results.

Figure 2.10 illustrates the robustness of the MBIR-BHC algorithm to sensor noise using the multi-material disk phantom. Our simulated data uses independent additive Gaussian noise with inverse variances given by (2.35) using $\lambda_{0,i} = 20000$ for all $i = 1, \cdots, M$ and $\sigma_e^2 = 16$. For the purposes of this particular comparison, we adjust the regularization in the MBIR-mono and MBIR-BHC to approximately match the noise variance of FBP. In practice, this means that the MBIR reconstructions are under-regularized since generally speaking MBIR can produce the same resolution as FPB at lower noise levels. Notice that both the FBP and MBIR-mono reconstructions

contain streaks, while the MBIR-BHC effectively removes the streak artifacts even in the presence of noise.

### The Modified NCAT Phantom

The third phantom we investigate is based on the NCAT phantom [48]. It has a FOV of 320 mm, and we manually inserted several regions of high and low density materials, such as soft tissue, bone, blood and metals, indicated in Figure 2.11. The densities and the mass attenuation coefficients of the materials used in the phantoms are obtained from the NIST XCOM database [49] and the chemical compositions of these materials are listed in Table 2.8 according to [50]. The simulated parallel-beam geometry has 1400 detectors with 0.23 mm spacing and 720 projection angles over 180 degrees. We do not simulate the noise and scatter effects. All the reconstructed images are 512×512. For MBIR-BHC, the 2-nd order polynomial model is used and the segmentation threshold $T$ is 800 HU.. The reconstruction results are shown in Figure 2.13.

Due to the presence of high density metal insertions, the FBP reconstruction exhibits several streaking artifacts crossing through the image, which degrades the overall image quality. While the generic MBIR-mono reconstruction generally improves the image quality and smooths out several degraded regions, it fails to eliminate the streaks connecting the high density regions, such as bone and metal. The EBHC method is not as effective on this data set, probably due to the presence of multiple high density objects. By comparison, the MBIR-BHC method dramatically reduces most of the streaking artifacts, while producing a better rendering in uniform regions and preserving the shape of edges as well. The difference between the reconstruction and the ground truth also demonstrates the effectiveness of MBIR-BHC in removing streaks. We also plot the mean pixel values of different regions in the phantom versus their theoretical values in Figure 2.12. In the low attenuation region, FBP, MBIR-mono and MBIR-BHC give roughly equal accuracy estimate, while EBHC tends to

Table 2.8: chemical composition of various materials used in the simulation

| material | density (g/cc) | chemical composition |
|---|---|---|
| water | 1.0 | $H_2O$ |
| soft tissue | 1.06 | H: 10.2%, C: 14.3%, N: 3.4%, O: 70.8%, Na: 0.2%, P: 0.3%, S: 0.3%, Cl: 0.2%, K: 0.3% |
| blood | 1.06 | H: 10.2%, C: 11.0%, N: 3.3%, O: 74.5%, Na: 0.1%, P: 0.1%, S: 0.2%, Cl: 0.3%, K: 0.2%, Fe: 0.1% |
| bone | 1.92 | H: 3.4%, C: 15.5%, N: 4.2%, O: 43.5%, Na: 0.1%, Mg: 0.2%, P: 10.3%, S: 0.3%, Ca: 22.5% |
| breast | 1.02 | H: 10.6%, C: 33.2%, N: 3.0%, O: 52.7%, Na: 0.1%, P: 0.1%, S: 0.2%, Cl: 0.1% |
| polyethylene | 0.93 | H: 14.372%, C: 85.628% |
| aluminum | 2.7 | Al |
| titanium | 4.506 | Ti |

under estimate the pixel value. In the high attenuation regions, all the methods pro-

duce lower accuracy estimates of density, but the MBIR-BHC method produces the most accurate results.

### 2.4.2 Real Scan Data Results

In this section, we apply different methods to a real X-ray CT scan dataset taken of actual baggage with high and low density objects. The dataset is acquired from the Imatron C300 CT scanner, provided by the ALERT DHS center, Northeastern University, USA. The parallel-beam sinogram has 1024 detectors with 0.46 mm spacing and 720 projection angles over 180 degrees, rebinned from a fan-beam scan. The projection data is water pre-corrected. The reconstructed images have a FOV of 475 mm with the resolution of 512×512. We use the 2-nd order MBIR-BHC and choose the segmentation threshold $T$ to be 800 HU.

We first investigate the convergence behavior of the MBIR-BHC algorithm. Figure 2.14(a) plots the objective function after each iteration of optimization over $x$, $b$ and $\gamma$. As we have described in Section 2.3, the objective function (2.40) is approximated by the quadratic approximation (2.43) using the second order Taylor series expansion with the expansion point iteratively refined during the reconstruction. While we point out that this approximation is not guaranteed to be an upper bound of the original objective function, which would ensure the convergence, we see from Figure 2.14(a) that in practice the objective function decreases, which suggests that the proposed strategy is effective for this high order non-linear optimization problem, and yields convergent results empirically. In Figure 2.14(b), we plot the change of the objective function relative to the converged value on a log scale, given by

$$\log\left(\frac{\text{cost}^{(t)} - \text{cost}^{(\infty)}}{\text{cost}^{(\infty)}}\right) \tag{2.64}$$

where $\text{cost}^{(\infty)}$ is the converged value of the objective function. Note that the change is also monotonic decreasing. Figure 2.14(c) plots the average pixel change after each iteration in log scale. and Figure 2.14(d) plots the coefficients of the correction polynomial after each iteration. As shown in the figures, the average pixel change

decreases to zero and the coefficients of the polynomial converge to a stable estimate after a few iterations.

Figure 2.15 shows the reconstruction results of this baggage scan dataset using different methods. By visual comparison to FBP and generic MBIR-mono, the MBIR-BHC method reduces the streaking and blooming artifacts significantly and produces reconstructions with higher resolution. This can be clearly observed in the zoomed-in region in Figure 2.16. The metal baggage handle causes a severe blooming artifact in the FBP image, and affects the nearby low density uniform regions as well. While the generic MBIR-mono algorithm recovers a few structures with better detail, it does not effectively address the artifacts due to the metal and many streaks remain on the final reconstructed image. On the other hand, the MBIR-BHC algorithm was able to produce more accurate and clearer structures. The streaking artifacts in the uniform attenuation regions, caused by the nearby high-density metal, are significantly reduced in the reconstructed images of the MBIR-BHC algorithm. Also, MBIR-BHC improves the overall resolution. Figure 2.15(d) illustrates the segmentation mask of MBIR-BHC after the reconstruction is finished. It can be observed that the algorithm correctly identifies the high density regions and eliminates the segmentation noise.

We also include the normalized error sinograms obtained from the generic MBIR-mono and MBIR-BHC algorithms in Figure 2.17 which illustrates the improvement of MBIR-BHC due to the proposed X-ray model with the polynomial parametrization. The normalized error sinogram is the difference between the sinogram data and the forward projection of the image, normalized by the weighting coefficients. If the forward model is correct and the reconstruction is a least-weighted-squares fit to the data, this normalized error should appear as approximately white noise with unit variance across the sinogram. Mathematically, for the generic MBIR algorithm, the normalized error sinogram is calculated as

$$e_i^{(\text{MBIR-mono})} = \sqrt{w_i}\left(y_i - \sum_{j=1}^{N} A_{i,j}x_j\right) \ , \tag{2.65}$$

and for the proposed MBIR-BHC algorithm, it is

$$e_i^{(\text{MBIR-BHC})} = \sqrt{w_i}(y_i - p_i) \ . \tag{2.66}$$

As seen from the figure, the MBIR-BHC shows a more uniform normalized error sinogram map with less fluctuation. Several traces due to the presence of the metal in the error sinogram of MBIR-mono nearly disappear in MBIR-BHC.

As seen from the results, MBIR-BHC has improved the overall image quality and significantly reduced the streaking artifacts due to beam hardening of the high density materials. Nonetheless, MBIR-BHC does not remove all beam-hardening artifacts. The remaining artifacts may be due to various reasons, including inaccurate modeling. For real scan data, other physical effects, such as scattering, may also influence the results. While Figure 2.6 indicates that the 2-nd order MBIR-BHC forward model is more accurate, the 3-rd order model shows little further improvement. This suggests that it may be possible to formulate different high-order models with less modeling error.

## 2.5 Conclusion

In this paper, we have presented a model-based iterative method for simultaneous image reconstruction and beam hardening correction (MBIR-BHC) which does not require any prior knowledge of the nonlinear characteristics of the system. The main idea is to jointly estimate the reconstruction and the beam hardening correction polynomial using an alternating optimization approach. The method is based on the assumption that distinct materials can be separated according to their densities. Under this assumption, the proposed method simultaneously estimates the reconstruction, the material segmentation mask, and the joint polynomial correction function of different material projections. Two separated projections are computed implicitly based on the low and high density materials during the iterative process. Therefore, no system information is needed and the correction is adapted to the dataset being used automatically. The experimental results on both the simulated

and real dataset demonstrated the efficiency of the proposed algorithm in reducing several artifacts in the reconstructed image, such as streaking.

## 2.6 Derivations of the Relationships in Section 2.2

In this appendix, we derive the equations (2.14), (2.24)-(2.25), and (2.29)-(2.31) in Section 2.2.

To see (2.14), we differentiate (2.11) and obtain

$$\begin{aligned}
\frac{d}{dp_i} f_{\mathcal{M}}(p_i)\Big|_{p_i=0} &= -\frac{\int_{\mathbb{R}} \tilde{S}(\mathcal{E}) \frac{d}{dp_i} e^{-r_{\mathcal{M}}(\mathcal{E})p_i} d\mathcal{E}}{\int_{\mathbb{R}} \tilde{S}(\mathcal{E}) e^{-r_{\mathcal{M}}(\mathcal{E})p_i} d\mathcal{E}}\Big|_{p_i=0} \\
&= \frac{\int_{\mathbb{R}} \tilde{S}(\mathcal{E}) e^{-r_{\mathcal{M}}(\mathcal{E})p_i} r_{\mathcal{M}}(\mathcal{E}) d\mathcal{E}}{\int_{\mathbb{R}} \tilde{S}(\mathcal{E}) e^{-r_{\mathcal{M}}(\mathcal{E})p_i} d\mathcal{E}}\Big|_{p_i=0} \\
&= \int_{\mathbb{R}} \tilde{S}(\mathcal{E}) r_{\mathcal{M}}(\mathcal{E}) d\mathcal{E} = 1
\end{aligned}$$

where the last equality is the result of (2.9).

To see (2.24), we differentiate (2.19) and obtain

$$\begin{aligned}
\gamma_{1,0} &= \frac{\partial}{\partial p_{L,i}} h(p_{L,i}, 0)\Big|_{p_{L,i}=0} \\
&= -\frac{\partial}{\partial p_{L,i}} \log\left(\int_{\mathbb{R}} \tilde{S}(\mathcal{E}) e^{-r_L(\mathcal{E})p_{L,i}} d\mathcal{E}\right)\Big|_{p_{L,i}=0} \\
&= \frac{\int_{\mathbb{R}} \tilde{S}(\mathcal{E}) e^{-r_L(\mathcal{E})p_i} r_L(\mathcal{E}) d\mathcal{E}}{\int_{\mathbb{R}} \tilde{S}(\mathcal{E}) e^{-r_L(\mathcal{E})p_i} d\mathcal{E}}\Big|_{p_{L,i}=0} \\
&= \int_{\mathbb{R}} \tilde{S}(\mathcal{E}) r_L(\mathcal{E}) d\mathcal{E} = 1
\end{aligned}$$

and (2.25) can be derived in the similar manner, changing the differentiation with respect to $p_{H,i}$.

For (2.29), plugging $p_{L,i} = p_{H,i} = 0$ into (2.27), we obatin

$$\tilde{\gamma}_{0,0} = f_{\mathcal{M}}^{-1}\left(-\log\left(\int_{\mathbb{R}} \tilde{S}(\mathcal{E}) e^0 d\mathcal{E}\right)\right) = f^{-1}(0) = 0\ . \tag{2.67}$$

Finally, to see (2.30), we apply the chain rule using (2.15) and (2.24) and obtain

$$\begin{aligned}\tilde{\gamma}_{1,0} &= \frac{\partial}{\partial p_{L,i}}\tilde{h}(p_{L,i},0)\Big|_{p_{L,i}=0} \\ &= \frac{df_{\mathcal{M}}^{-1}(h(p_{L,i},0))}{dh(p_{L,i},0)}\frac{\partial}{\partial p_{L,i}}h(p_{L,i},0)\Big|_{p_{L,i}=0} \\ &= \int_{\mathbb{R}}\tilde{S}(\mathcal{E})r_L(\mathcal{E})d\mathcal{E} = 1\end{aligned}$$

and (2.31) can be derived in the similar manner, changing the differentiation with respect to $p_{H,i}$.

## 2.7 Derivation of the ICD Update Equations

In this appendix, we derive the ICD pixel update in detail. We rewrite (2.40) as a function of the pixel $x_j$, drop the terms which are independent of $x_j$, and obtain the 1D optimization problem over $x_j$ given by

$$\begin{aligned}x_j = \arg\min_{u\geq 0}\Bigg\{&\theta_1(u-\tilde{x}_j)+\frac{1}{2}\theta_2(u-\tilde{x}_j)^2 \\ &+\beta\left((u-T)_+(1-b_j)+(T-u)_+b_j\right) \\ &+\sum_{k\in\partial j}\alpha_{j,k}\rho(u-x_k)\Bigg\}\end{aligned} \tag{2.68}$$

where $\tilde{x}_j$ is the previous pixel value and $\theta_1$ and $\theta_2$ are given by (2.49) and (2.50). Following the similar strategy in [38], we simplify the optimization by replacing the function $\rho$ with a quadratic substitute functional $q$ given by

$$q(u-x_k;\tilde{x}_j-x_k) = a_{j,k}(u-x_k)^2 + C_{j,k} \tag{2.69}$$

where $a_{j,k}$ and $C_{j,k}$ are given by

$$a_{j,k} = \frac{\rho'(\tilde{x}_j-x_k)}{2(\tilde{x}_j-x_k)}\,, \tag{2.70}$$

$$C_{j,k} = \rho(\tilde{x}_j-x_k)-\frac{a_{j,k}}{2}(\tilde{x}_j-x_k)^2\,. \tag{2.71}$$

It can be easily shown that this function $q$ is an upper bound of $\rho$, satisfying the two constraints given by

$$q(u - x_k; \tilde{x}_j - x_k) \geq \rho(u - x_k) \ , \tag{2.72}$$

$$q(\tilde{x}_j - x_k; \tilde{x}_j - x_k) = \rho(\tilde{x}_j - x_k) \ . \tag{2.73}$$

Therefore, such substitution will not alter the optimal solution when the algorithm converges. Substituting (2.69) into (2.68) and dropping the terms which do not depend on $u$, we obtain the 1D optimization (2.47) with $\alpha'_{j,k}$ given by (2.48).

To derive the optimal solution to (2.47), we separate the cases when $b_j = 0$ or 1. We first suppose $b_j = 0$ and zero the derivative of (2.47) to obtain the normal equation given by

$$\begin{aligned} \theta_1 - \theta_2 \tilde{x}_j - 2 \sum_{k \in \partial j} \alpha'_{j,k} x_k &+ \left( \theta_2 + 2 \sum_{k \in \partial j} \alpha'_{j,k} \right) u \\ &= -\beta \text{step}(u - T) \\ D_1 + D_2 u &= -\beta \text{step}(u - T) \end{aligned} \tag{2.74}$$

where step$(\cdot)$ is the unit step function, and $D_1$ and $D_2$ are given by (2.51) and (2.52). The solution to (2.74) can be obtained using the shrinkage operator in solving LASSO and $l_1$ regularized problems [51], and the closed form solution is given by (2.53). For the case when $b_j = 1$, we have the normal equation given by

$$D_1 + D_2 u = \beta \text{step}(T - u) \ . \tag{2.75}$$

and the update equation in this case becomes (2.55). Figure 2.18 illustrates these two cases graphically.

$x \leftarrow$ from FBP or generic MBIR

$b \leftarrow$ initially segment $x$ using (2.57)

**for** $i = 1$ to $M$ **do**

  $p_i \leftarrow$ calculate using (2.20) and (2.21)

  $\hat{p}_i \leftarrow p_i$

**end for**

**repeat**

  $\gamma \leftarrow$ solution of (2.41)

  **for** $i = 1$ to $M$ **do**

    $d^{(i)}, Q^{(i)} \leftarrow$ calculate using (2.44) and (2.45)

  **end for**

  **for** $j = 1$ to $N$ **do**

    $x_j \leftarrow$ calculate using ICDUpdate in Figure 2.2

  **end for**

  **for** $j = 1$ to $N$ **do**

    $b_j \leftarrow$ solution of (2.58)

    $p_i \leftarrow$ updated using (2.59)

  **end for**

  **for** $i = 1$ to $M$ **do**

    $\hat{p}_i \leftarrow p_i$

  **end for**

**until** convergence

Fig. 2.3.: Pseudocode of the MBIR-BHC algorithm for simultaneous image reconstruction and beam hardening correction. First, we initialize the reconstruction $x$ and the segmentation $b$, and compute $\hat{p}_i$ for all $i$. Then, the algorithm iterates and for each iteration, the optimal coefficient $\hat{\gamma}$ is first calculated followed by the calculation of the parameters $d^{(i)}$ and $Q^{(i)}$ for all $i$. After that, the optimal $x$ is solved by minimizing the quadratic approximation (2.43) and the optimal segmentation $b$ is estimated using ICM. Finally, the expansion point is updated which will be used in the next iteration.

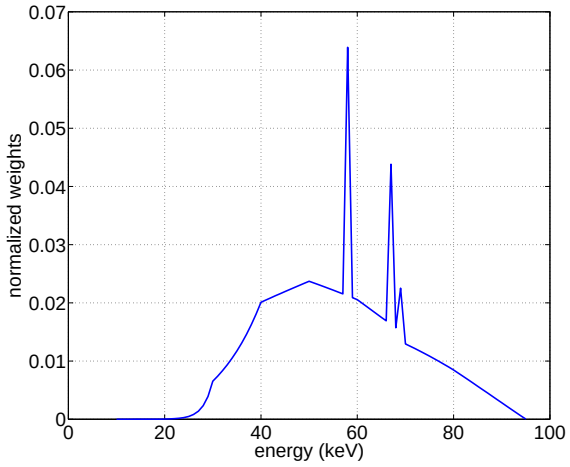


Fig. 2.4.: Normalized energy spectrum of the X-ray source used for simulation

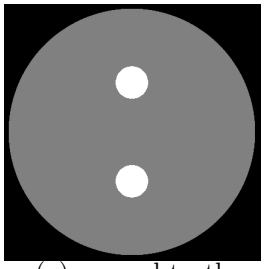

(a) ground truth

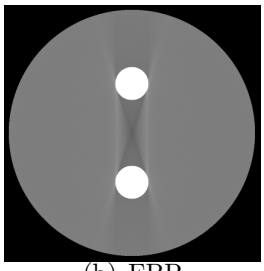

(b) FBP

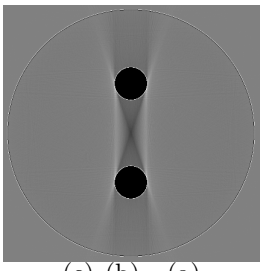

(c) (b) - (a)

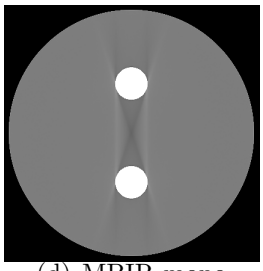

(d) MBIR-mono

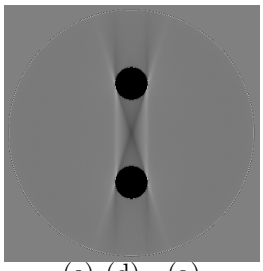

(e) (d) - (a)

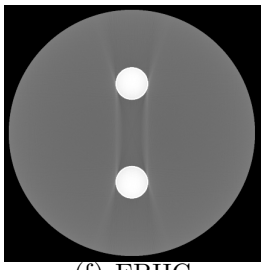

(f) EBHC

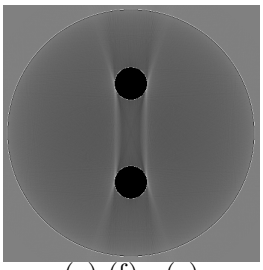

(g) (f) - (a)

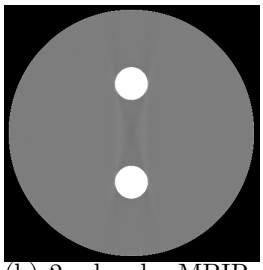

(h) 2-nd order MBIR-BHC

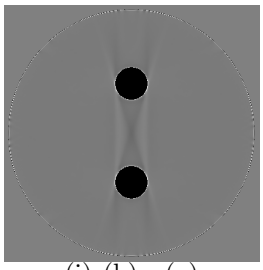

(i) (h) - (a)

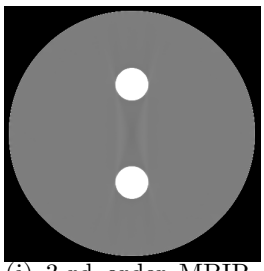

(j) 3-rd order MBIR-BHC

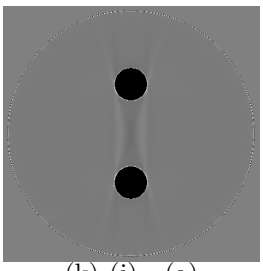

(k) (j) - (a)

Fig. 2.5.: Comparison of FBP, MBIR-mono, EBHC and 2-nd and 3-rd order MBIR-BHC reconstructed images. Top row: the reconstructed images. Bottom row: the difference images. The display window for the reconstructed images is [-400 400] HU. The display window for the difference images is [-200 200] HU. Notice that the MBIR-BHC algorithm reduces visible beam-hardening artifacts in the reconstruction of simulated data.

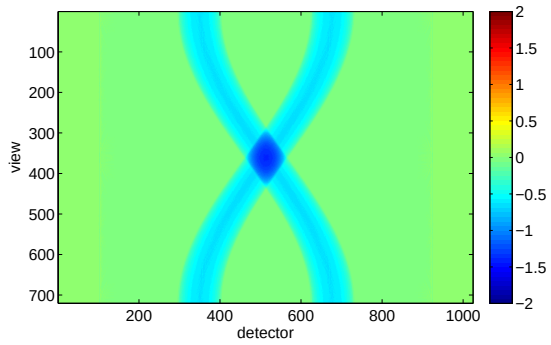


(a) MBIR-mono

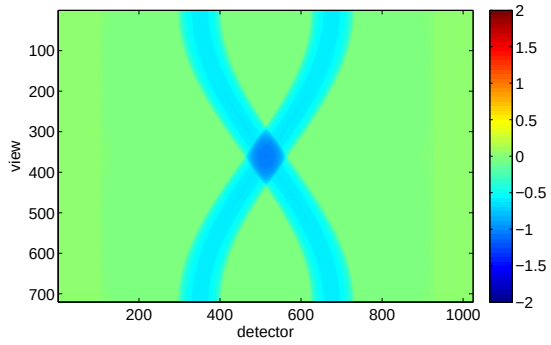


(b) 2-nd order MBIR-BHC

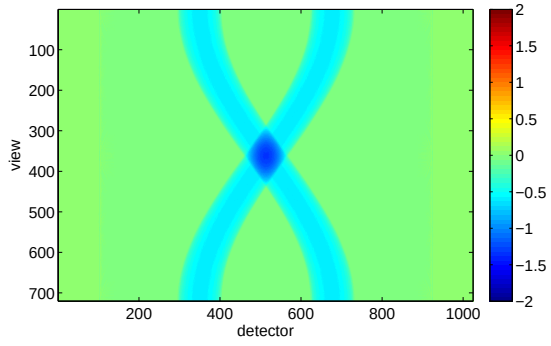


(c) 3-rd order MBIR-BHC

Fig. 2.6.: Comparison of the modeling error for the three forward models of MBIR-mono, MBIR-BHC with a 2-nd order model, and MBIR-BHC with a 3-rd order model. Notice that MBIR-BHC with the second order model produces the smallest modeling error.

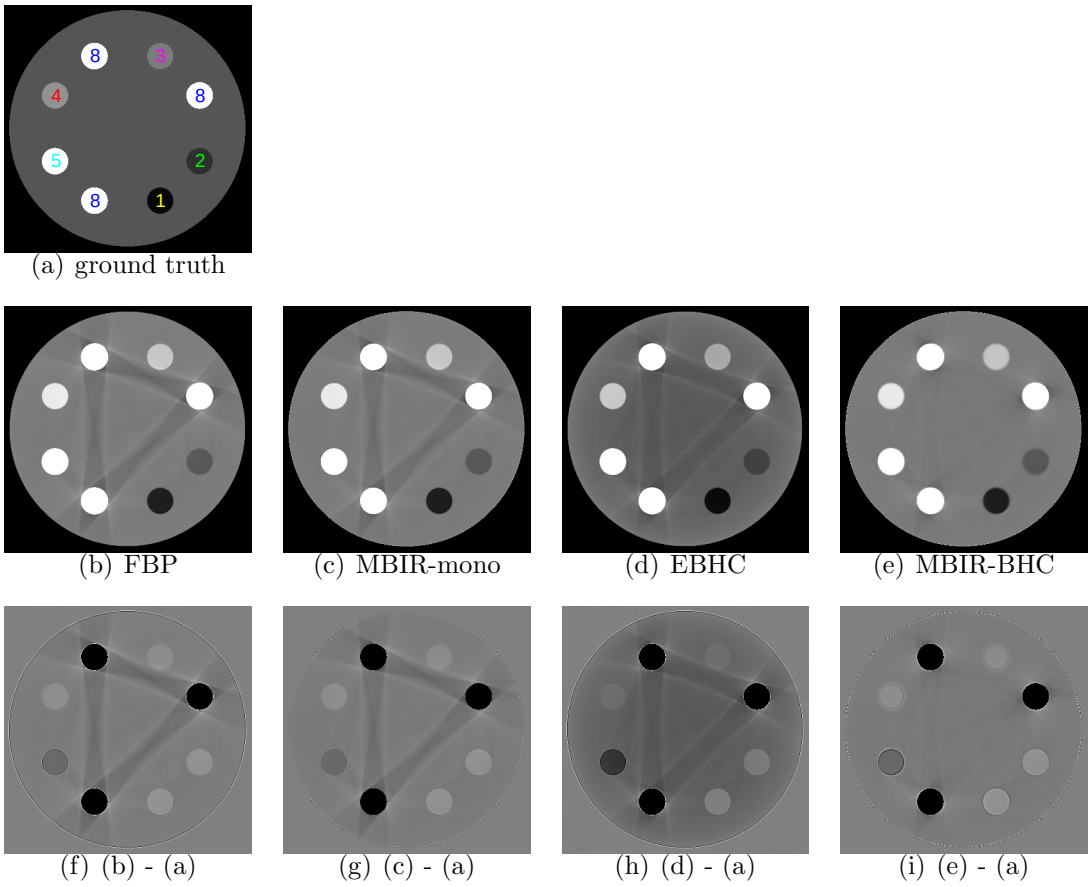


(a) ground truth

(b) FBP (c) MBIR-mono (d) EBHC (e) MBIR-BHC

(f) (b) - (a) (g) (c) - (a) (h) (d) - (a) (i) (e) - (a)

Fig. 2.7.: Comparison of FBP, MBIR-mono, EBHC and MBIR-BHC reconstructed images. Top row: the reconstructed images. Bottom row: the difference images. The display window for the reconstructed images is [-200 200] HU. The display window for the difference images is [-200 200] HU. Notice that the MBIR-BHC algorithm reduces visible beam-hardening artifacts in the reconstruction of simulated data.

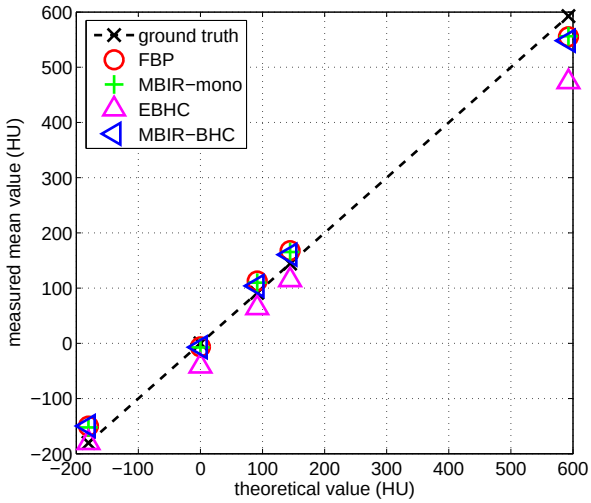


Fig. 2.8.: Comparison of the reconstruction accuracy of FBP, MBIR-mono, EBHC and MBIR-BHC. Ground truth values are calculated using (2.6). Notice that the MBIR-BHC reconstruction algorithm produces relatively low bias in the reconstructed density.

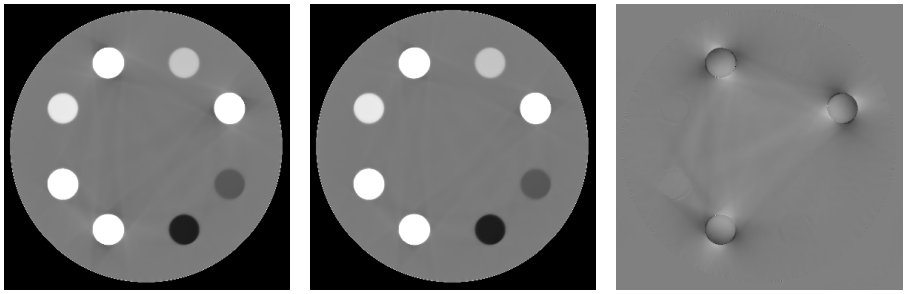

(a) 2-nd order MBIR-BHC (b) 3-rd order MBIR-BHC (c) (b) - (a)

Fig. 2.9.: Comparison of 2-nd order MBIR-BHC and 3-rd order MBIR-BHC. The display window for the reconstructed images is [-200 200] HU. The display window for the difference image is [-50 50] HU. Notice that the 2-nd order model produces good results with lower complexity than the 3-rd order model.

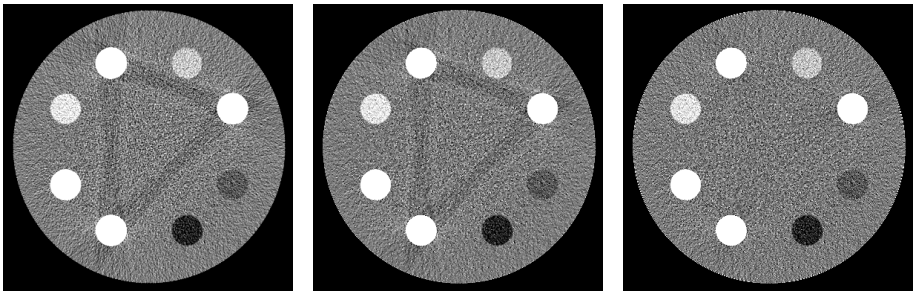

(a) FBP (b) MBIR-mono (c) MBIR-BHC

Fig. 2.10.: Comparison of FBP, MBIR-mono and MBIR-BHC reconstructions on noisy sinogram. The display window for the reconstructed images is [-200 200] HU. Notice that the MBIR-BHC algorithm robustly removes beam-hardening artifacts in the presence of simulated measurement noise.

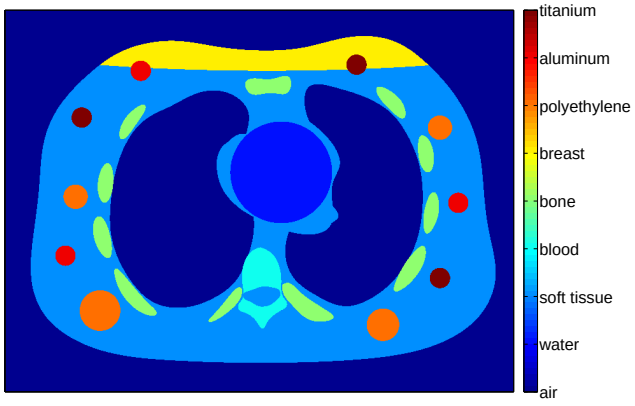


(a) chemical composition

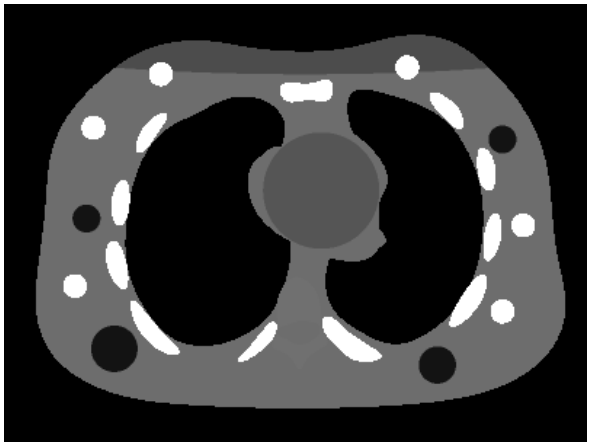

(b) attenuation map

Fig. 2.11.: The material composition of the modified NCAT phantom. Top row: color-coded material composition of the phantom. Bottom row: the attenuation map of the phantom. The display window is [-200, 400] HU.

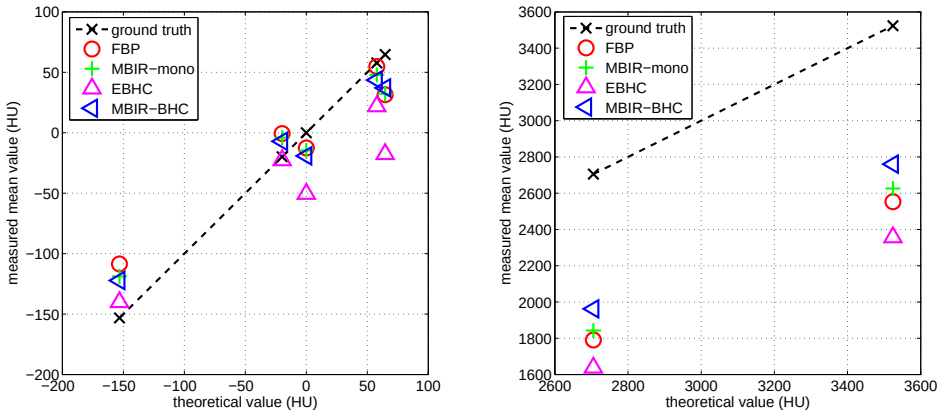


(a) low attenuation region (b) high attenuation region

Fig. 2.12.: Comparison of the reconstruction accuracy of FBP, MBIR-mono, EBHC and MBIR-BHC on NCAT phantom. Ground truth values are calculated using (2.6). Notice that the MBIR-BHC reconstruction algorithm produces the lowest bias in estimated density among the tested algorithms.

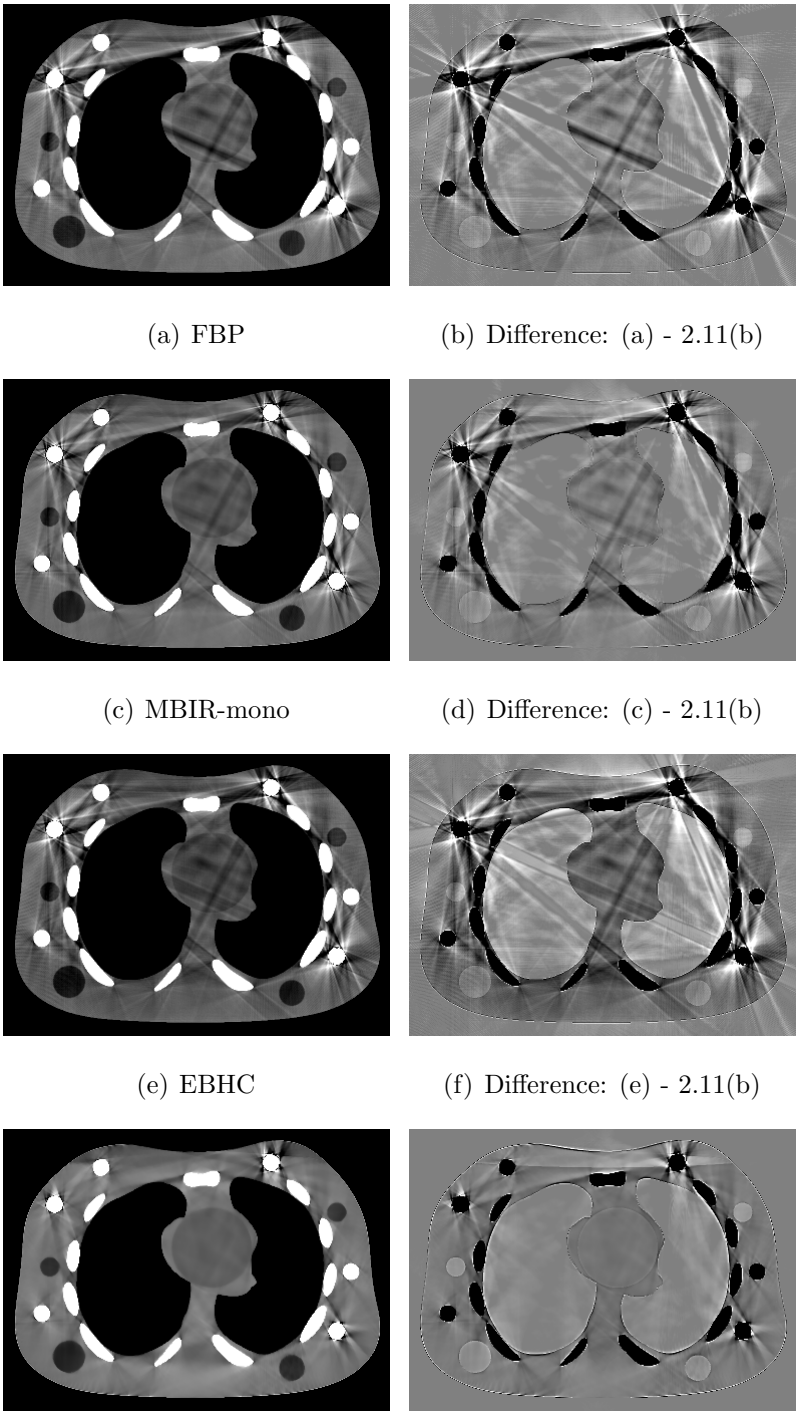

(a) FBP (b) Difference: (a) - 2.11(b)

(c) MBIR-mono (d) Difference: (c) - 2.11(b)

(e) EBHC (f) Difference: (e) - 2.11(b)

(g) MBIR-BHC (h) Difference: (g) - 2.11(b)

Fig. 2.13.: Comparison of FBP, the generic MBIR with mono-energetic X-ray model (MBIR-mono), and MBIR-BHC reconstructed images. First row: the reconstructed images. Second row: the difference images. The display window for the reconstructed images is [-200 400] HU. The display window for the difference images is [-200 200] HU. Notice that the MBIR-BHC algorithm reduces visible beam-hardening artifacts in the reconstruction of the simulated human phantom.

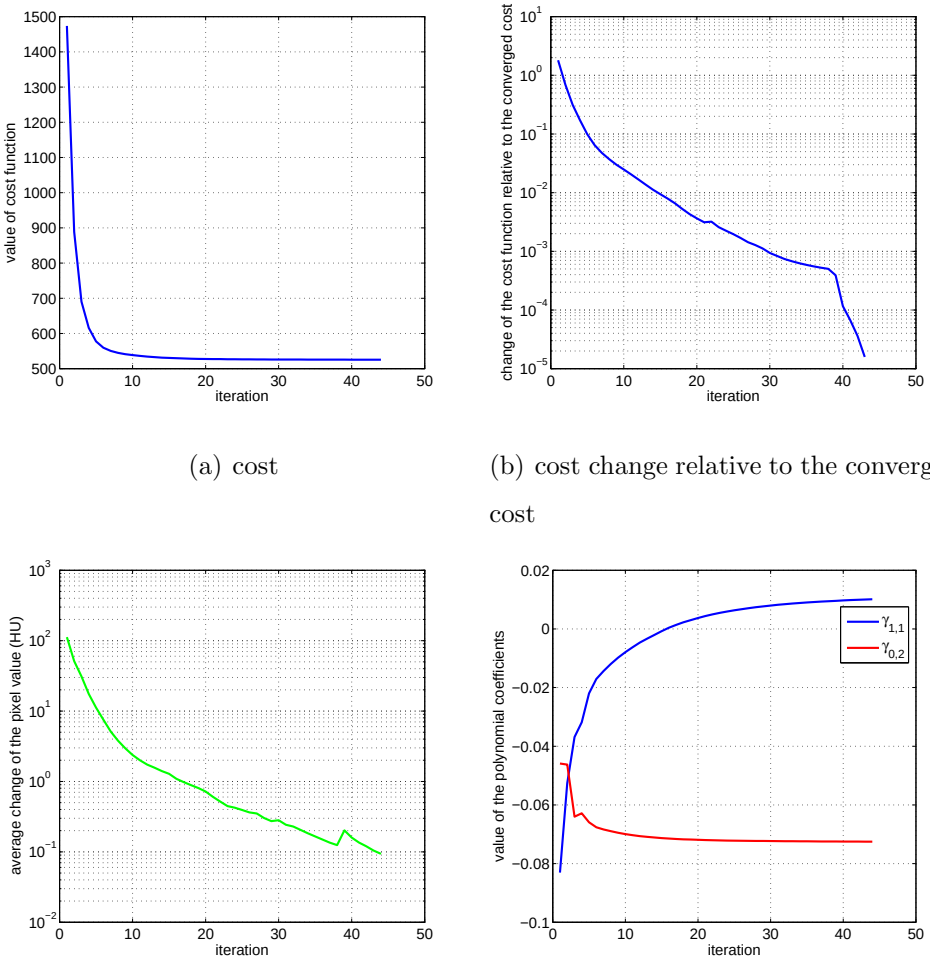


(a) cost

(b) cost change relative to the converged cost

(c) average pixel change

(d) polynomial coefficients

Fig. 2.14.: Convergence of MBIR-BHC algorithm. The plots show (a): value of the exact objective function of (2.40), (b): the change of the objective function relative to the converged value (c): the average change of pixel value, (d): estimated polynomial coefficients, after each iteration.

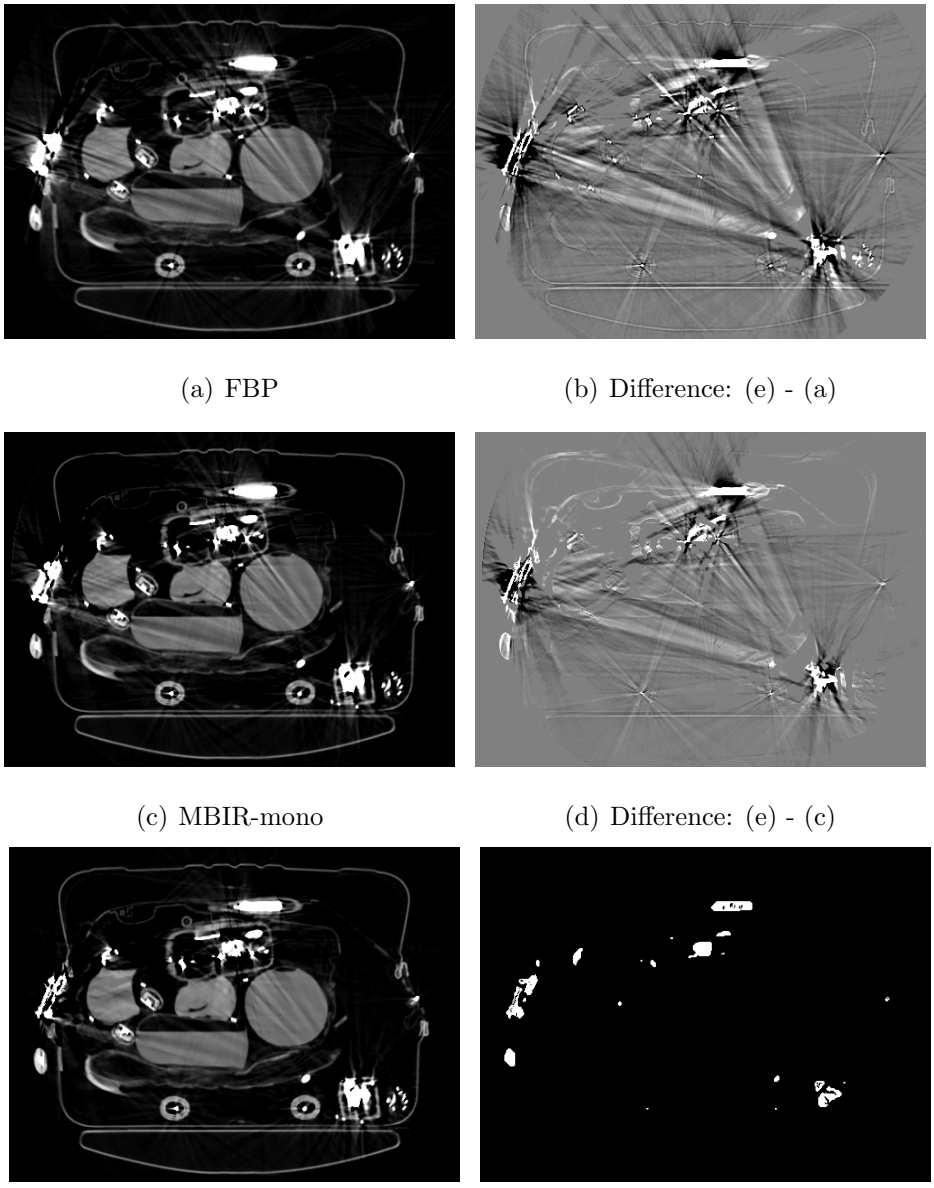

(a) FBP (b) Difference: (e) - (a)

(c) MBIR-mono (d) Difference: (e) - (c)

(e) MBIR-BHC algorithm (f) MBIR-BHC segmentation mask

Fig. 2.15.: Comparison of FBP, the generic MBIR with mono-energetic X-ray model (MBIR-mono), MBIR-BHC, on the real X-ray CT data of a scanned baggage. Top row: the reconstructed images. Bottom row shows the segmentation mask of MBIR-BHC and difference images between MBIR-BHC and FBP, difference between MBIR-BHC and MBIR-mono. The display window for the reconstructed images (a)-(c) is $[-1000, 1000]$ HU. The display window for the difference images (d)-(e) is $[-500, 500]$ HU In (d), white pixels indicate the pixels which are classified as the high density materials in MBIR-BHC. Notice that the MBIR-BHC algorithm reduces visible beam-hardening artifacts such as streaking on this real data set.

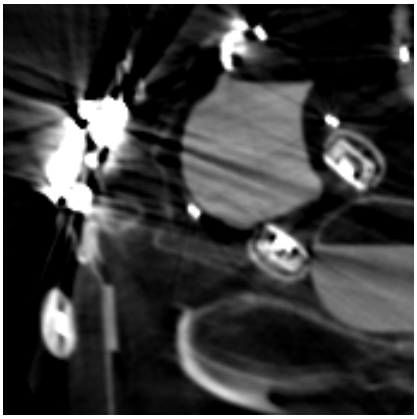

(a) FBP

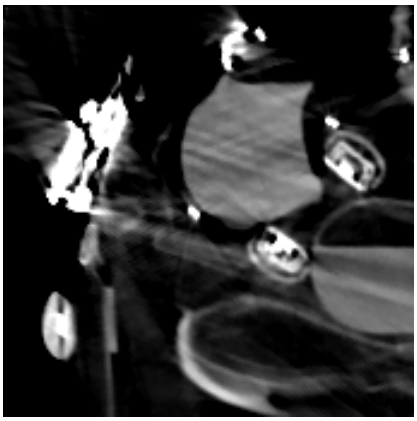

(b) MBIR-mono

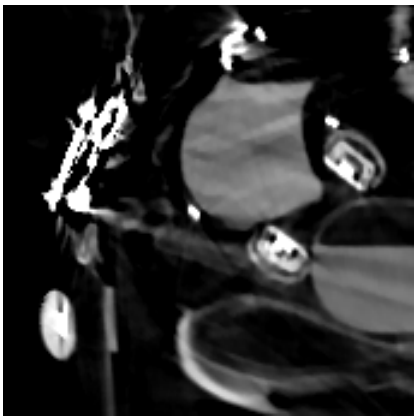

(c) MBIR-BHC

Fig. 2.16.: Comparison of FBP, MBIR-mono, MBIR-BHC on the real X-ray CT data of a scanned baggage. Images are zoomed-in a region including metal objects. The display window is $[-1000, 1000]$ HU. Notice that the MBIR-BHC reconstructions have reduced streaking, more uniform homogeneous regions, and less blooming of metal in this real data set.

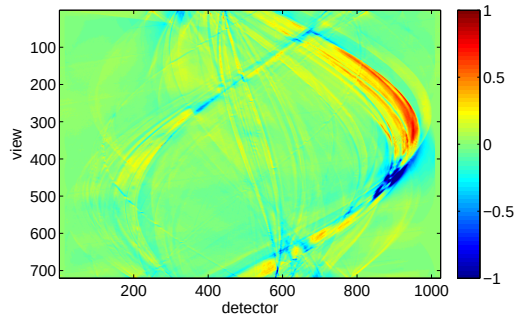


(a) MBIR-mono

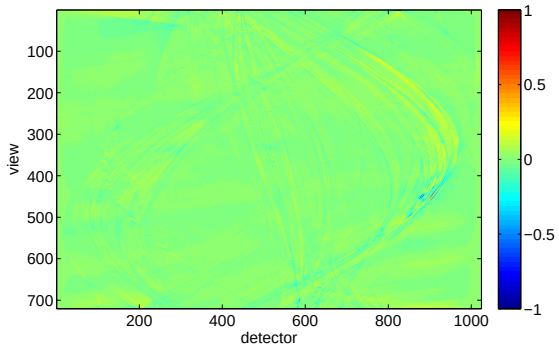


(b) MBIR-BHC

Fig. 2.17.: Comparison of MBIR-mono and MBIR-BHC on the normalized error sinogram

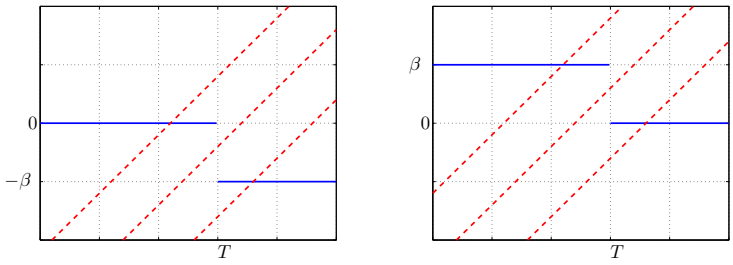


(a) $b_j = 0$ (b) $b_j = 1$

Fig. 2.18.: Illustration of the solutions of (2.74) and (2.75). The blue solid lines depict the right side of the normal equations. The red dashed lines depict the left side of the normal equations for different $D_1$ and $D_2$. The solutions are the intersections of the blue and red lines.

# 3. JOINT METAL ARTIFACT REDUCTION AND SEGMENTATION FOR CT IMAGES

## 3.1 Introduction

Computed Tomography (CT) has a wide range of applications in medical diagnosis [1] and security inspection [41]. In many of these applications, it is important and necessary to segment CT images for further analysis. For example, segmentation of anatomical structure is a critical step in image guided radiotherapy or the design of custom bone replacements. Segmentation is also of great importance in security applications where objects are segmented before target classification.

However, raw CT images often contain artifacts such as streaks due to dense metal objects, and these artifacts can make accurate segmentation difficult. In the past decades, people have developed various metal artifact reduction (MAR) techniques to correct the image. Perhaps the most well-known approaches in MAR are based on sinogram correction (SC-MAR). These methods typically correct the metal trace in the raw CT data by using either sinogram inpainting [52, 53] or the knowledge obtained from the projection of a prior image that is derived from the original CT image [54, 55]. The final image of SC-MAR is then produced by reconstructing the corrected sinogram. Alternatively, if the original CT data is not available, MAR can be done in the image domain (ID-MAR). Some ID-MAR methods produce the corrected image by utilizing a pseudo sinogram from the projection of the original CT image [53]. Others identify the metal artifact regions in the image and apply image restoration techniques to do the correction [56].

On the other side, there have also been a variety of methods proposed for segmentation by using graph cut [57], shape prior [58], active contour [59], Mumford-Shah functional [60] etc.. Perhaps, the most related work in the CT application is [61],

which is based on the method of isoperimetric graph partitioning [62]. The algorithm searches for splits within the connected components recursively until it is unable to find a strong separation. However, it does not fully explore the metal artifact structure in the CT image. Surprisingly, while a great deal of research has been done in metal artifact reduction and segmentation as individual tasks, relatively little research has considered the two problems jointly.

In this chapter, we propose a novel approach to the segmentation of CT images with metal artifacts, and with no access to the raw CT data [63]. Our method is based on the joint estimation of both the segmentation and the restored image in a unified optimization framework. The unified cost function consists of three terms: 1) a data fidelity term that relates the raw and restored image and incorporates a streak mask; 2) a dictionary-based image prior which regularizes the restored image; 3) a term based on the continuous-relaxed Potts model which couples the restored image intensities and segmentation labels. We derive an alternating optimization algorithm to minimize the overall cost function and the result of this procedure produces a joint segmentation and restoration of the image. We present results on both simulated and real CT data and demonstrate that the joint MAR and segmentation can produce better results than the separated ID-MAR and segmentation method, without the use of the raw CT data.

## 3.2 Joint Metal Artifact Reduction and Segmentation

Let $x^{(\text{orig})} \in \mathbb{R}^N$ be the input CT image with metal artifacts. Assume $K$ target material intensities $\mu \in \mathbb{R}^K$ is given and a binary artifact mask $b \in \{0,1\}^N$, defined as

$$b_i = \begin{cases} 1 & \text{if the } i\text{-th pixel has artifact} \\ 0 & \text{otherwise} \end{cases}, \tag{3.1}$$

is obtained in advance. Our objective is to use $x^{(\text{orig})}$, $\mu$ and $b$ to produce an output image $x$ which has reduced metal artifacts and a segmentation label vector $z \in \{1, \cdots, K\}^N$ of $K$ materials over the image.

We formulate this problem as the joint optimization problem of the restored image and segmentation. Mathematically, the overall cost function can be written as

$$\min_{x,z} \left\{ \frac{1}{2} \sum_{i=1}^{N} (1 - b_i)(x_i - x_i^{(\text{orig})})^2 + J_I(x) \right. \\ \left. + \frac{\beta}{2} \sum_{i=1}^{N} \sum_{k=1}^{K} w_i \delta(z_i - k)(x_i - \mu_k)^2 + \lambda \sum_{\{i,j\} \in \mathcal{C}} (1 - \delta(z_i - z_j)) \right\} \quad (3.2)$$

where $\delta(\cdot)$ is the delta function, $\mathcal{C}$ represents the set of all neighboring pixel pairs, and $\beta$, $\lambda$ are the regularization weights. Here $J_I(x)$ denotes the image domain prior which is used to balance the local smoothness and edge structures. We also add the weights $w_i$, defined as

$$w_i = \begin{cases} w & \text{if } b_i = 1 \\ 1 & \text{if } b_i = 0 \end{cases}, \quad (3.3)$$

to control the segmentation term in artifact and non-artifact regions.

Notice that the optimization over the segmentation label $z$ only involves the last two terms, which is essentially the MAP segmentation based on the discrete Potts model. However, due to the non-convexity, this solution can often be trapped into a local minimum which can lead to poor segmentation result. Instead, we use an approach similiar to [64] and propose a continuous-relaxed version of the discrete Potts model. In particular, we relax the $\delta(z_i - k)$ to be a probability measure $u_i$ for each $i$, and the overall problem becomes the following constrained optimization:

$$\min_{x,u} \left\{ \frac{1}{2} \sum_{i=1}^{N} (1 - b_i)(x_i - x_i^{(\text{orig})})^2 + J_I(x) \right. \\ \left. + \frac{\beta}{2} \sum_{i=1}^{N} \sum_{k=1}^{K} w_i u_{i,k} (x_i - \mu_k)^2 + \lambda \sum_{\{i,j\} \in \mathcal{C}} \sum_{k=1}^{K} |u_{i,k} - u_{j,k}| \right\}$$

$$\text{subject to } \; 0 \le u_{i,k} \le 1, \; \sum_{k=1}^{K} u_{i,k} = 1 \; . \quad (3.4)$$

Once we have the optimal $u$, the segmentation label can be obtained by picking up the label with the largest probability,

$$z_i \leftarrow \arg \max_{k \in \{1,\cdots,K\}} u_{i,k} \ . \tag{3.5}$$

Lastly, the image domain prior $J_I(x)$ regularizes the local image behavior and serves to fill in correct pixel values in the metal artifact region. Several priors have been proposed in different image processing applications.We construct the term $J_I(x)$ by representing all the overlapped patches as the sparse combination of entries from a globally learned dictionary $\Phi$ using the similar approach in [65]. Loosely speaking, it assumes that

$$R_i x \approx \Phi \nu_i, \quad \text{with} \quad \|\nu_i\|_0 \leq T \tag{3.6}$$

where $\Phi$ is the global over-complete dictionary, $R_i$ is the matrix to extract a patch located at the $i$-th pixel, $\nu_i$ is the corresponding sparse coefficient vector, and $T$ is the specified sparsity constraint. Under certain conditions [66, 67], it is equivalent to solve an unconstrained optimization with the $l_0$ norm replaced by $l_1$. Substituting the image prior into $J_I(x)$ in (3.4), we obtain the final optimization problem as follows

$$\begin{aligned} \min_{x,u,\nu} \Bigg\{ & \frac{1}{2} \sum_{i=1}^{N} (1 - b_i)(x_i - x_i^{(\text{orig})})^2 + \frac{\alpha}{2} \sum_{i=1}^{N} \|R_i x - \Phi \nu_i\|_2^2 + \sum_{i=1}^{n} \gamma_i \|\nu_i\|_1 \\ & + \frac{\beta}{2} \sum_{i=1}^{N} \sum_{k=1}^{K} w_i u_{i,k} (x_i - \mu_k)^2 + \lambda \sum_{\{i,j\} \in \mathcal{C}} \sum_{k=1}^{K} |u_{i,k} - u_{j,k}| \Bigg\} \\ & \text{subject to} \ \ 0 \leq u_{i,k} \leq 1, \ \sum_{k=1}^{K} u_{i,k} = 1 \end{aligned} \tag{3.7}$$

where $\alpha$ and $\gamma_i$ are additional regularization weights.

We use alternating optimizing to solve (3.7). The inputs of the algorithm are the original image $x^{(\text{orig})}$, the artifact mask $b$, the globally learned dictionary $\Phi$ for image patches, the mean intensities $\mu$ of $K$ materials, and the regularization weights $\alpha$, $\beta$, $\gamma_i$ and $w_i$. At the initialization step, we set the image $x \leftarrow x^{(\text{orig})}$, and $u_{i,k} \leftarrow \frac{1}{K}$ for all $i$ and $k$. Firstly, fixing $x$ and $u$, optimization over $\nu$ can be solved patch-wise using the standard sparse coding techniques, such as Orthogonal Matching Pursuit

(OMP) [68]. Then, with $\nu$ and $u$ fixed, we optimize over the image $x$. If we denote $U \in \mathbb{R}^{N\times K}$ as the matrix whose entries are $u_{i,k}$, $W$ and $D$ as the diagonal matrices whose diagonal entries are $w_i$ and $1-b_i$ respectively, then the image update can be written in the compact form as

$$\min_x \left\{ \frac{1}{2}\|x - x^{(\text{orig})}\|_D^2 + \frac{\alpha}{2}\sum_{i=1}^{N} \|R_i x - \Phi\nu_i\|_2^2 + \frac{\beta}{2}\|x - U\mu\|_W^2 \right\}, \tag{3.8}$$

and its solution is given by

$$x \leftarrow \Big(D + \beta W + \alpha \sum_{i=1}^{N} R_i^T R_i\Big)^{-1}\Big(Dx^{(\text{orig})} + \beta W U\mu + \alpha \sum_{i=1}^{N} R_i^T \Phi\nu_i\Big) \tag{3.9}$$

Despite its complicated form, (3.9) is nothing but the weighted average of all the overlapped patches with some additional pixel-wise regularization, and the update in (3.9) can be implemented very efficiently using pixel-wise division. Finally, fixing $\nu$ and $x$, we solve the constrained optimization over $u$ given by

$$\min_u \left\{ \frac{\beta}{2}\|x - U\mu\|_W^2 + \lambda \sum_{\{i,j\}\in\mathcal{C}} \sum_{k=1}^{K} |u_{i,k} - u_{j,k}| \right\}$$

$$\text{subject to } \; 0 \le u_{i,k} \le 1, \; \sum_{k=1}^{K} u_{i,k} = 1 \; . \tag{3.10}$$

The optimization (3.10) can be solved using the effective continuous max-flow algorithm in [64], which the min-cut problem into the convex optimization problem.

### 3.3 Identify Metal Artifacts in CT Images

We next describe a simple method to generate the artifact mask $b$ for CT images with metal artifacts. We propose the forward and backward projection method to generate the binary artifact mask $b$ as follows.

- Step 1: Generate the high density image $x^{(\text{high})}$

$$x_i^{(\text{high})} \leftarrow x_i^{(\text{orig})}\delta\Big(x_i^{(\text{orig})} \ge L^{(\text{high})}\Big) \tag{3.11}$$

  where $L^{(\text{high})}$ is the threshold for high density pixels.

- Step 2: Apply the forward Radon transform to $x^{(\text{orig})}$ and $x^{(\text{high})}$ separately to obtain two projections:

$$p^{(\text{high})} \leftarrow Ax^{(\text{high})}, \;\; p^{(\text{orig})} \leftarrow Ax^{(\text{orig})} \tag{3.12}$$

  where $A$ represents the forward projection matrix.

- Step 3: Correct the high density projection

$$p_i^{(\text{corr})} = \frac{p_i^{(\text{high})}}{p_i^{(\text{orig})}} p_i^{(\text{high})^r} = \frac{p_i^{(\text{high})^{1+r}}}{p_i^{(\text{orig})}} \tag{3.13}$$

- Step 4: Apply Filter Back-projection (FBP) to the corrected projection and thresholding.

$$b' \leftarrow \text{FBP}\Big(p^{(\text{corr})}\Big) \tag{3.14}$$

$$b \leftarrow \delta\Big(b'_i > L^{(\text{artifact})}\Big)\delta\Big(x_i^{(\text{orig})} < L^{(\text{high})}\Big) \tag{3.15}$$

  where $L^{(\text{artifact})}$ is the threshold for metal artifact pixels.

## 3.4 Results

We compare the proposed method with the method where the image is first passed through an image restoration algorithm [69] for metal artifact reduction, and then applied to the continuous-relaxed Potts model segmentation [64].

The first dataset is a simulated dataset based on the NCAT phantom [48]. The ground truth intensity and segmentation maps are shown in Figure 3.1. The raw CT image is shown in Figure 3.2(b), and the generated artifact mask is shown in Figure 3.2(a). We use K-SVD algorithm on $9 \times 9$ patches from the raw image with the sparsity $T = 3$ to train a global dictionary. The input mean intensities are $\mu = [0, 850, 1100, 3500, 4700]^T$ HU. Figure 3.2 shows the comparison of different methods. The raw CT image in Figure 3.2(b) contains many streak artifacts due to metal, and the resulting segmentation in Figure 3.2(c) is inaccurate in the artifact regions. In Figure 3.2(d) and 3.2(e), while applying the restoration followed by segmentation

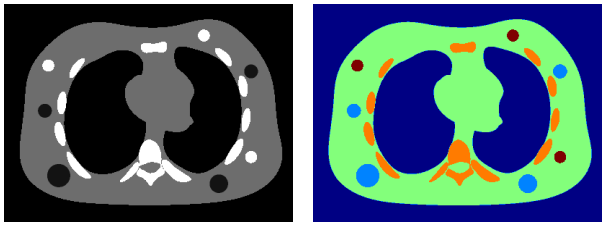

(a) (b)

Fig. 3.1.: the ground truth (a) intensity map, (b) segmentation, of the simulated data, the display window of the intensity is $[-200, 400]$ HU; the segmentation label is color-coded.

| Method | RMSE (HU) | Sørensen-Dice score [70] |
|---|---|---|
| baseline | 136.9830 | 0.8828 |
| squential MAR/seg. | 167.2736 | 0.9135 |
| joint MAR/seg. | 99.3498 | 0.9382 |

Table 3.1: Quantitative comparison of different methods. The Dice score are averaged over all the labels.

can reduce some artifacts, it is sensitive to the mask and can not generate a good segmentation directly. In contrast, the output of the proposed algorithm in Figure 3.2(f) and 3.2(g) gives better results. Major metal artifacts are reduced and the segmentation is more accurate. The quantitative result in Table 3.1 also suggests the proposed method generates better image and segmentation.

The second dataset is a real baggage CT image in a security application. Figure 3.3(b) shows the raw image, which contains strong streak artifacts due to the metal in the bag and Figure 3.3(a) shows the artifact mask. We set the mean intensities to be $\mu = [0, 600, 1000, 1150, 1400, 3000]^T$ HU. Figure 3.3(c) shows the segmentation on the raw CT image and notice that objects are split due to the streak artifact. Figure 3.3(d) and 3.3(e) show the results of applying the restoration algorithm followed by

segmentation separately. While the restoration algorithm fills in the correct values in some artifact regions, it introduces extra artifacts, such as the region around the thin sheet on top left. This leads to the inaccurate segmentation in Figure 3.3(e). On the other side, the major metal streak artifacts are corrected in the output image of the proposed algorithm in Figure 3.3(f). Furthermore, the alternating optimization algorithm merges the objects that were originally split and produces a more accurate segmentation in Figure 3.3(g).

## 3.5 Conclusions

In this paper, we consider the problem of segmentation of CT images with metal artifacts and with no access to the CT data. We present a novel approach based on a joint estimation over image and segmentation in an unified optimization framework. The cost function includes a dictionary-based image prior, and a continuous-relaxed Potts model for multi-class segmentation. By alternating optimization, the algorithm is able to improve both the image quality and segmentation simultaneously. Results on both simulated and read datasets show that the method is very effective in reducing metal artifact and producing better segmentation than the separated ID-MAR and segmentation method, without the use of the raw CT data.

(a)

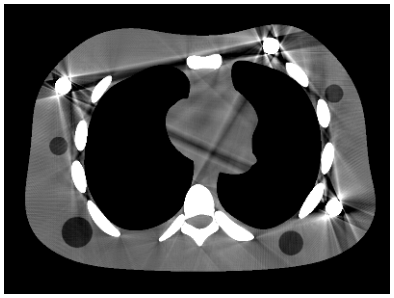

(b)

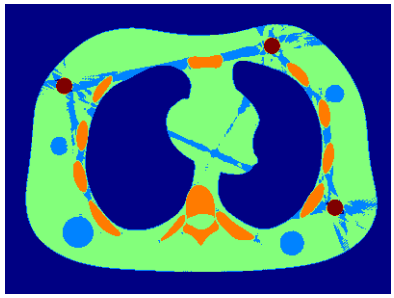

(c)

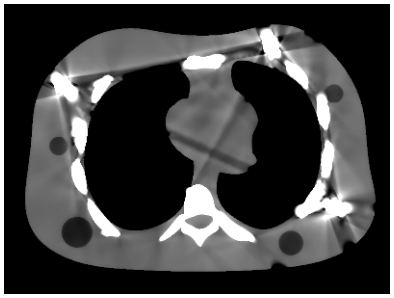

(d)

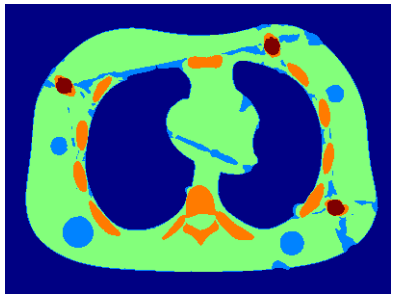

(e)

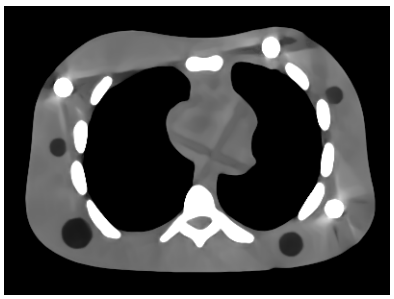

(f)

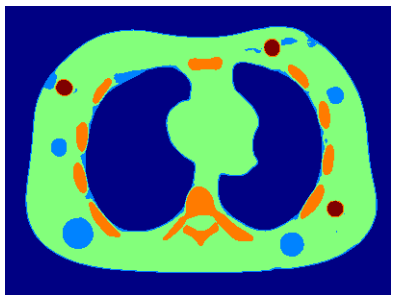

(g)

Fig. 3.2.: (a) the generated artifact mask, (b) the raw CT image, (c) the segmentation on (b), (d) the output image by applying an image domain restoration, (e) the segmentation on (d), (f) the output image of the proposed algorithm, (g) the segmentation of the proposed algorithm, the display window is $[-200, 400]$ HU; the segmentation is color-coded.

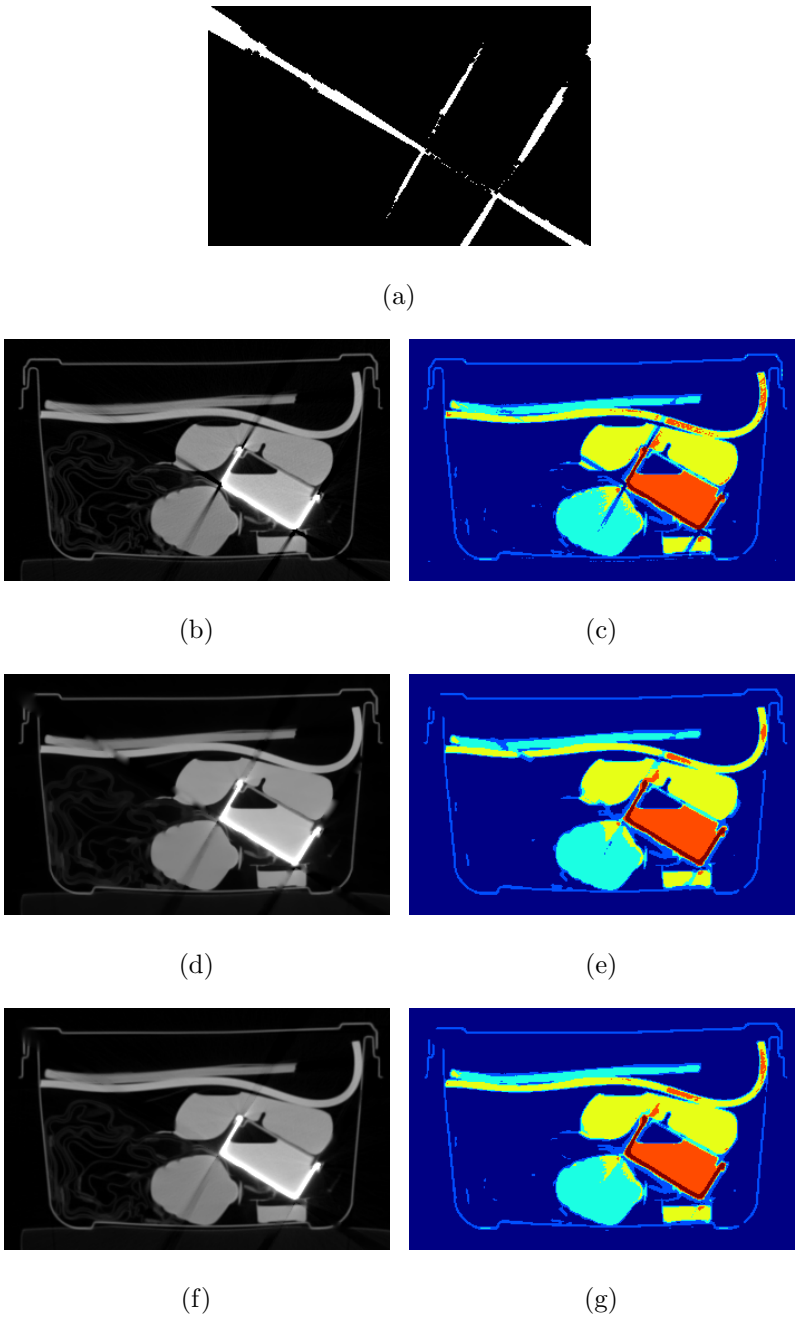

(a)

(b) (c)

(d) (e)

(f) (g)

Fig. 3.3.: (a) the generated artifact mask, (b) the raw CT baggage scan image, (c) the segmentation on (b), (d) the image by applying an image domain restoration, (e) the segmentation on (d), (f) the output image of the proposed algorithm, (g) the segmentation of the proposed algorithm; the display window is $[-1000, 1000]$ HU; the segmentation is color-coded.

# LIST OF REFERENCES

# LIST OF REFERENCES


[1] J.-B. Thibault, K. D. Sauer, C. A. Bouman, and J. Hsieh, "A three-dimensional statistical approach to improved image quality for multislice helical CT," *Med. Phys.*, vol. 34, pp. 4526–4544, Nov. 2007.

[2] K. D. Sauer and C. A. Bouman, "A local update strategy for iterative reconstruction from projections," *IEEE Trans. Signal Process.*, vol. 41, pp. 534–548, Feb. 1993.

[3] B. D. Man and S. Basu, "Distance-driven projection and backprojection in three dimensions," *Phys. Med. Biol.*, vol. 49, no. 11, pp. 2463–2475, 2004.

[4] C. A. Bouman and K. D. Sauer, "A unified approach to statistical tomography using coordinate descent optimization," *IEEE Trans. Image Process.*, vol. 5, pp. 480–492, Mar. 1996.

[5] J. D. Ingle and S. R. Crouch, *Spectrochemical Analysis*. Prentice Hall, first ed., 1988.

[6] R. A. Brooks and G. D. Chiro, "Beam hardening in X-ray reconstructive tomography," *Phys. Med. Biol.*, vol. 21, no. 3, pp. 390–398, 1976.

[7] J. Hsieh, *Computed Tomograhpy: Principles, Design, Artifacts, and Recent Advances*, ch. 7, pp. 270–279. Wiley, second ed., 2009.

[8] W. D. McDavid, R. G. Waggener, W. H. Payne, and M. J. Dennis, "Spectral effects on three-dimensional reconstruction form X-rays," *Med. Phys.*, vol. 2, no. 6, pp. 321–324, 1975.

[9] L. M. Zatz and R. E. Alvarez, "An inaccuracy in computed tomography: the energy-dependence of CT values," *Radiology*, vol. 124, pp. 91–97, July 197.

[10] A. J. Duerinckx and A. Macovski, "Polychromatic streak artifacts in computer tomography images," *Journal of Computer Assisted Tomography*, vol. 2, pp. 481–487, Sept. 1978.

[11] P. S. Rao and R. J. Alfidi, "The environmental density artifact: a beam-hardening effect in computed tomography," *Radiology*, vol. 141, pp. 223–227, Oct. 1981.

[12] W. D. McDavid, R. G. Waggener, W. H. Payne, and M. J. Dennis, "Correction for spectral artifacts in cross-sectional reconstruction from X rays," *Med. Phys.*, vol. 4, no. 1, pp. 54–57, 1977.

[13] S. C. Pang and S. Genna, "Correction for X-ray polychromaticitiy effects on three-dimensional reconstruction," *IEEE Trans. Nucl. Sci.*, vol. 23, pp. 623–626, Feb. 1976.

[14] G. T. Herman, "Correction for beam hardening in computed tomography," *Phys. Med. Biol.*, vol. 24, no. 1, pp. 81–106, 1979.

[15] R. E. Alvarez and A. Macovski, "Energy-selective reconstructions in X-ray computerized tomography," *Phys. Med. Biol.*, vol. 21, no. 5, pp. 733–744, 1976.

[16] J. P. Stonestrom, R. E. Alvarez, and A. Macovski, "A framework for spectral artifact corrections in X-ray CT," vol. 28, pp. 128–141, Feb. 1981.

[17] P. M. Joseph and R. D. Spital, "A method for correcting bone induced artifacts in computed tomography scanners," *Journal of Computer Assisted Tomography*, vol. 20, pp. 100–108, Jan. 1978.

[18] "A method of iterative data refinement and its applications," *Mathematical Methods in Applied Science*, vol. 7, pp. 108–123, 1985.

[19] G. Herman and S. Trivedi, "A comparative study of two postreconstruction beam hardening correction methods," *IEEE Trans. Med. Imag.*, vol. 2, pp. 128–135, Sept. 1983.

[20] P. M. Joseph and C. Ruth, "A method for simultaneous correction of spectrum hardening artifacts in CT images containing both bone and iodine," *Med. Phys.*, vol. 24, pp. 1629–1634, Oct. 1997.

[21] J. Hsieh, R. Molthen, C. A. Dawson, and R. H. Johnson, "An iterative approach to the beam hardening correction in cone beam CT," *Med. Phys.*, vol. 27, pp. 23–29, Jan. 2000.

[22] A. J. Coleman and M. Sinclair, "A beam-hardening correction using dual-energy computed tomography," *Phys. Med. Biol.*, vol. 30, no. 11, pp. 1251–1256, 1985.

[23] R. J. Jennings, "A method for comparing beam-hardening filter materials for diagnostic radiology," *Med. Phys.*, vol. 15, no. 4, pp. 588–599, 1988.

[24] O. Nalcioglu and R. Y. Lou, "Post-reconstruction method for beam hardening in computerised tomography," *Phys. Med. Biol.*, vol. 24, no. 2, pp. 330–340, 1979.

[25] C. H. Yan, R. T. Whalen, G. S. Beaupré, S. Y. Yen, and S. Napel, "Reconstruction algorithm for polychromatic CT imaging: Application to beam hardening correction," *IEEE Trans. Med. Imag.*, vol. 19, pp. 1–11, Jan. 2000.

[26] B. D. Man, J. Nuyts, P. Dupont, G. Marchal, and P. Suetens, "An iterative maximum-likelihood polychromatic algorithm for CT," *IEEE Trans. Med. Imag.*, vol. 20, pp. 998–1008, Oct. 2001.

[27] I. A. Elbakri and J. A. Fessler, "Statistical X-ray computed tomography image reconstruction with beam hardening correction," in *Proc. of SPIE Conf. on Medical Imaging: Image Processing*, vol. 4322, 2001.

[28] I. A. Elbakri and J. A. Fessler, "Segmentation-free statistical image reconstruction for polyenergetic X-ray computed tomography with experimental validation," *Phys. Med. Biol.*, vol. 48, pp. 2453–2477, Aug. 2003.

[29] E. V. de Casteele, D. V. Dyck, J. Sijbers, and E. Raman, "A model-based correction method for beam hardening artefacts in X-ray microtomograhpy," *Journal of X-Ray Science and Technology*, vol. 12, no. 1, pp. 43–57, 2004.

[30] S. Srivastava and J. A. Fessler, "Simplified statistical image reconstruction algorithm for polyenergetic X-ray CT," in *Proc. of IEEE Nucl. Sci. Symp.*, pp. 1551–1555, 2005.

[31] M. Kachelrieß, K. Sourbella, and W. A. Kalender, "Empirical cupping correction: A first-order raw data pre-correction for cone-beam computed tomography," *Med. Phys.*, vol. 37, pp. 1269–1274, May 2006.

[32] H. Gao, L. Zheng, Z.-Q. Chen, Y. Xing, and S. Li, "Beam hardening correction for middle-energy industrial computerized tomograhpy," *IEEE Trans. Nucl. Sci.*, vol. 53, pp. 2796–2807, Oct. 2006.

[33] M. Krumm, K. Kasperl, and M. Franz, "Reducing non-linear artifacts of multi-material objects in industrial 3d computed tomography," *NDT & E International*, vol. 41, no. 4, pp. 242–251, 2008.

[34] M. Abella and J. A. Fessler, "A new statistical image reconstruction algorithm for polyenergetic X-ray CT," in *Proc. of IEEE Int'l. Symp. Biomed. Imag.*, pp. 165–168, 2009.

[35] Y. Kyriakou, E. Meyer, D. Prell, and M. Kachelrieß, "Empirical beam hardening correction (EBHC) for CT," *Med. Phys.*, vol. 37, pp. 5179–5187, Oct. 2010.

[36] M. Krumm, K. Kasperl, and M. Franz, "Beam hardening correction of multi-material objects," in *10-th European Conference on Non-Destructive Testing*, 2010.

[37] J. M. Verburg and J. Seco, "CT metal artifact reduction method correcting for beam hardening and missing projections," *Phys. Med. Biol.*, vol. 57, pp. 2803–2818, Apr. 2012.

[38] Z. Yu, J.-B. Thibault, C. A. Bouman, K. D. Sauer, and J. Hsieh, "Fast model-based X-ray CT reconstruction using spatially nonhomogenenous ICD optimization," *IEEE Trans. Image Process.*, vol. 20, pp. 161–175, Jan. 2011.

[39] R. Zhang, J.-B. Thibault, C. A. Bouman, K. D. Sauer, and J. Hsieh, "Model-based iterative reconstruction for dual-energy X-ray CT using a joint quadratic likelihood model," *IEEE Trans. Med. Imag.*, vol. 33, pp. 117–134, Jan. 2014.

[40] S. J. Kisner, P. Jin, C. A. Bouman, K. D. Sauer, W. Garms, T. Gable, S. Oh, M. Merzbacher, and S. Skatter, "Innovative data weighting for iterative reconstruction in a helical ct security baggage scanner," in *IEEE Int'l Carnahan Conf. on Security Technology*, (Medellín, Colombia), 2013.

[41] P. Jin, E. Haneda, C. A. Bouman, and K. D. Sauer, "A model-based 3D multi-slice helical CT reconstruction algorithm for transportation security application," in *Proc. 2nd Intl. Mtg. on image formation in X-ray CT*, pp. 297–300, 2012.

[42] P. Jin, C. A. Bouman, and K. D. Sauer, "A method for simultaneous image reconstruction and beam hardening correction," in *Conference Record of IEEE Nuclear Science Symposium and Medical Imaging Conference*, (Seoul, Korea), Nov. 2013.

[43] P. Jin, K. D. Sauer, and C. A. Bouman, "A model-based image reconstruction algorithm with simultaneous beam hardening correction for X-ray CT," *to appear IEEE Transaction on Computational Imaging*.

[44] A. Mohammad-Djafari, "Joint estimation of parameters and hyperparameters in a bayesian approach of solving inverse problems," in *IEEE Int'l. Conf. Image Proc.*, vol. 2, (Lausanne), pp. 473–476, Sept. 1996.

[45] A. B. Milstein, S. Oh, K. J. Webb, C. A. Bouman, Q. Zhang, D. A. Boas, and R. P. Millane, "Fluorescence optical diffusion tomography," *Applied Optics*, vol. 42, pp. 3081–3094, June 2003.

[46] P. Jin, E. Haneda, and C. A. Bouman, "Implicit gibbs prior models for tomographic reconstruction," in *the 46th Asilomar Conference on Signals, Systems and Computers*, (Pacific Grove, CA), pp. 613–616, Nov. 2012.

[47] K. Cranley, B. J. Gilmore, G. W. A. Fogarty, and L. Deponds, "Catalogue of diagnostic X-ray spectra and other data," Tech. Rep. 78, IPEM Report (The Institute of Physics and Engineering in Medicine), York, 1997.

[48] W. P. Segars, M. Mahesh, T. J. Beck, E. C. Frey, and B. M. W. Tsui, "Realistic CT simulation using the 4D XCAT phantom," *Med. Phys.*, vol. 35, pp. 3800–3808, Aug. 2008.

[49] NIST, "Tables of X-ray mass attenuation coefficients and mass energy absorption coefficients." Available from http://www.nist.gov/pml/data/xraycoef/index.cfm.

[50] ICRU, "Tissue substitutes in radiation dosimetry and measurement," Tech. Rep. 44, ICRU Report (The Interntaional Commission on Radiation Units and Measurements), Bethesda, MD, 1989.

[51] R. Tibshirani, "Regression shrinkage and selection via the Lasso," *J. R. Statist. Soc.*, vol. 58, no. 1, pp. 267–288, 1996.

[52] Y. Kim, S. Yoon, and J. Yi, "Effective sinogram-inpainting for metal artifact reduction in X-ray ct images," in *IEEE Conf. Image Processing (ICIP)*, pp. 597–600, 2010.

[53] H. K. Tuy, "A post-processing algorithm to reduce metallic clip artifacts in CT images," *Eur. Radiol.*, no. 3, pp. 129–134, 1993.

[54] E. Meyer, R. Raupach, M. Lell, B. Schmidt, and M. Kachelriess, "Normalized metal artifact reduction (NMAR) in computed tomography," *Medical Physics*, pp. 5482–5493, Oct. 2010.

[55] E. Meyer, R. Raupach, M. Lell, B. Schmidt, and M. Kachelriess, "Frequency split metal artifact reduction (FSMAR) in computed tomography," *Medical Physics*, pp. 1904–1916, Apr. 2012.

[56] A. Anderla, D. Culibrk, G. Delso, and M. Mirkovic, "MR image based approach for metal artifact reduction in x-ray ct," *The Scientific World Journal*, 2013.

[57] Y. Boykov and V. Kolmogorov, "An experimental comparison of min-cut/max-flow algorithms for energy minimization in vision," *IEEE Trans. Pattern Analysis and Machine Intelligence*, vol. 26, pp. 1124–1137, Sept. 2004.

[58] N. Vu and B. S. Manjunath, "Shape prior segmentation of multiple objects with graph cuts," in *IEEE Conf. Computer Vision and Pattern Recognition (CVPR)*, 2008.

[59] W. Yu, P. Franchetti, Y. Chang, and T. Chen, "Fast and robust active contours for image segmentation," in *IEEE Conf. Image Processing (ICIP)*, pp. 641–644, 2010.

[60] J. An and Y. Chen, "Region based image segmentation using a modified Mumford-Shah algorithm," in *Scale Space and Variational Methods in Computer Vision*, pp. 733–742, 2007.

[61] L. Grady, V. Singh, T. Kohlberger, C. Alvino, and C. Bahlmann, "Automatic segmentation of unknown objects, with application to baggage security," in *Eur. Conf. Computer Vision (ECCV)*, pp. 430–444, 2012.

[62] L. Grady and E. L. Schwartz, "Isoperimetric graph partitioning for image segmentation," *IEEE Trans. Pattern Analysis and Machine Intelligence*, vol. 28, no. 3, pp. 469–475, 2006.

[63] P. Jin, D. H. Ye, and C. A. Bouman, "Joint metal artifact reduction and segmentation of ct images using dictionary-based image prior and continuous-relaxed potts model," in *IEEE Int'l. Conf. Image Proc.*, (Québec), Sept. 2015.

[64] J. Yuan, E. Bae, X. C. Tai, and Y. Boykov, "A continuous max-flow approach to Potts model," in *Eur. Conf. Computer Vision (ECCV)*, 2010.

[65] M. Aharon, M. Elad, and A. Bruckstein, "K-SVD: An algorithm for designing overcomplete dictionaries for sparse representation," *IEEE Trans. Signal Proc.*, vol. 54, no. 11, pp. 4311–4322, 2006.

[66] D. L. Donoho, M. Elad, and V. Templyakov, "Stable recovery of sparse overcomplete representation in the presence of noise," *IEEE Trans. Info. Thoery*, vol. 52, no. 1, pp. 6–8, 2006.

[67] J. A. Tropp, "Just relax: Convex programming methods for subset selection and sparse approximation," *IEEE Trans. Info. Thoery*, vol. 51, no. 3, pp. 1030–1051, 2005.

[68] Y. C. Pati, R. Rezaiifar, and P. S. Krishnaprasad, "Orthogonal matching pursuit: Recursive function approximation with applications to wavelet decomposition," in *the 27th Asilomar Conference on Signals, Systems and Computers*, (Pacific Grove, CA), 1993.

[69] D. Garcia, "Robust smoothing of gridded data in one and higher dimensions with missing values," *Computational Statistics and Data Analysis*, vol. 54, pp. 1167–1178, 2010.

[70] L. R. Dice, "Measures of the amount of ecologic association between species," *Ecology*, vol. 26, no. 3, pp. 297–302, 1945.

VITA

# VITA

Pengchong Jin received his Bachelor of Engineering degree in Electronic and Computer Engineering from The Hong Kong University of Science and Technology (HKUST), Hong Kong, in 2009, and he is currently pursuing his Ph.D. degree in the School of Electrical and Computer Engineering, Purdue University, West Lafayette, Indiana. He has been with Integrated Imaging Laboratory at Purdue University under the direction of Prof. Charles A. Bouman since January 2010. In summer 2014, he was interned at Google Inc., Mountain View, working on video compression research. His current research interests include image processing, computational imaging, computer vision and machine learning with applications in tomography, camera imaging and photography.